Contents lists available at ScienceDirect

Bioactive Materials

Creating a bionic scaffold via light-curing liquid crystal ink to reveal the role of osteoid-like microenvironment in osteogenesis

Kun Liu [a], Lin Li [a], Yizhi Li [a], Yiting Luo [a], Zhaoyu Zhang [a], Wei Wen [a,b], Shan Ding [a,b], Yadong Huang [c], Mingxian Liu [a,b], Changren Zhou [a,b], Binghong Luo [a,b,*]

[a] Biomaterial Research Laboratory, Department of Material Science and Engineering, College of Chemistry and Materials, Jinan University, Guangzhou, 510632, PR China
[b] Engineering Research Center of Artificial Organs and Materials, Ministry of Education, Guangzhou, 510632, PR China
[c] Department of Cell Biology & Institute of Biomedicine, College of Life Science and Technology, Guangzhou, 510632, PR China

ABSTRACT

Osteoid plays a crucial role in directing cell behavior and osteogenesis through its unique characteristics, including viscoelasticity and liquid crystal (LC) state. Thus, integrating osteoid-like features into 3D printing scaffolds proves to be a promising approach for personalized bone repair. Despite extensive research on viscoelasticity, the role of LC state in bone repair has been largely overlooked due to the scarcity of suitable LC materials. Moreover, the intricate interplay between LC state and viscoelasticity in osteogenesis remains poorly understood. Here, we developed innovative hydrogel scaffolds with osteoid-like LC state and viscoelasticity using digital light processing with a custom LC ink. By utilizing these LC scaffolds as 3D research models, we discovered that LC state mediates high protein clustering to expose accessible RGD motifs to trigger cell-protein interactions and osteogenic differentiation, while viscoelasticity operates via mechanotransduction pathways. Additionally, our investigation revealed a synergistic effect between LC state and viscoelasticity, amplifying cell-protein interactions and osteogenic mechanotransduction processes. Furthermore, the interesting mechanochromic response observed in the LC hydrogel scaffolds suggests their potential application in mechanosensing. Our findings shed light on the mechanisms and synergistic effects of LC state and viscoelasticity in osteoid on osteogenesis, offering valuable insights for the biomimetic design of bone repair scaffolds.

1. Introduction

Osteoid creates an ideal microenvironment for osteogenesis *in vivo* due to its unique viscoelasticity and liquid crystal (LC) state, which are pivotal in directing cell behavior and regulating osteogenesis [1,2]. Replicating osteoid characteristics stands as one of the most effective strategies in scaffold design for bone tissue engineering. Extensive research has focused on the influence of viscoelasticity of osteoid on cell behavior and fate, particularly within viscoelastic hydrogels. Grolman et al. reported that the fate of bone marrow mesenchymal stem cells (BMSCs) closely correlates with the modulus of the osteoid, identifying a modulus threshold of 9–17 kPa for osteogenic differentiation of stem cells [3–5]. Stem cells tend toward osteogenic differentiation above this threshold, while adipose tissue and chondrocyte differentiation are favored below. Liu et al. designed a viscoelastic gelatin methacryloyl

hydrogel with tunable stiffness and loss modulus by utilizing small molecules as "bridges", demonstrating that hydrogels with higher loss modulus are beneficial to promote osteogenic differentiation [6]. Stress relaxation, a typical attribute of viscoelastic matrices, has also been shown to influence the behavior and fate of BMSCs, with hydrogels exhibiting shorter stress relaxation time proving more conducive to stem cell spreading and osteogenic differentiation [2,7–9]. While these findings elucidate the impact of osteoid viscoelasticity on cells, LC state remains overlooked in the aforementioned seminal studies.

The interplay between LC state and viscoelasticity is integral to the properties of osteoid. Despite significant attention on viscoelasticity, the distinct LC state of osteoid has received scant exploration. A primary hindrance to this investigation is the scarcity of LC materials mimicking osteoid characteristics. While some researchers have experimented with LC collagen extracted from tissues for bone repair, its application has

---

been limited to two-dimensional (2D) cell culture matrices due to its inadequate mechanical properties and demanding LC formation conditions [10–12]. Liquid crystal elastomers (LCEs) have emerged as a potential avenue for developing LC materials, encompassing both 2D films and 3D cell scaffolds. However, concerns regarding cytotoxicity, non-degradability, and temperature sensitivity have hampered the utilization of LCEs in bone tissue engineering [13–15]. Thus, the quest for novel LC materials is imperative to investigate the role of LC state in osteoid. Chitin whiskers (CHW), characterized by high aspect ratio, possess the ability to self-assemble into a cholesteric LC texture under mechanical forces (Figs. S1 and S2). Recently, a type of osteoid-like hydrogel was developed by embedding a polymer network into the LC helical topology of CHW [16–18], demonstrating significant enhancement in osteogenic differentiation of stem cells in a 2D microenvironment. However, the challenge lies in constructing a standalone viscoelastic hydrogel scaffold with osteoid LC state, owing to the poor mechanical properties and limited crosslinking efficiency of these hydrogels. Consequently, LC hydrogels were integrated into the pores of 3D printing PLLA scaffolds to augment bone regeneration [16], albeit exhibiting mechanical characteristics closer to the PLLA scaffold than the LC hydrogel itself. This composite scaffold fails to replicate the 3D viscoelastic and LC state microenvironment of osteoid. Thus, the mechanisms underlying LC state and viscoelasticity in directing cell behaviors, osteogenic differentiation, and osteogenesis remain largely unexplored, leaving unanswered questions regarding their potential synergistic role.

In addition to considering viscoelasticity and LC state, the processing method of hydrogel-based bone tissue engineering scaffolds is also crucial. An ideal scaffold for bone tissue engineering should feature large pores and 3D channel structures conducive to cell migration, nutrient penetration, and the ingrowth of new blood vessels during bone regeneration. However, the weak mechanical strength of hydrogels presents a challenge in fabricating 3D hydrogel scaffolds with optimal microstructures and morphologies, necessitating strict requirements for hydrogel molding technology. The emergence of 3D printing technology not only enables the manufacture of porous hydrogel scaffolds but also allows for personalized customization to address specific bone defects. Among the various 3D printing technologies, digital light processing (DLP) stands out as an effective means of constructing 3D hydrogel scaffolds. However, DLP printing of LC hydrogel scaffolds with an osteoid-like microenvironment is still lacking. Ink design plays a crucial role in addressing this gap. The ideal ink should not only possess an osteoid-like LC state but also exhibit a suitable photocrosslinking rate and viscosity to enable DLP printing.

Here, we developed a rapid photocrosslinking polyethylene glycol dimethacrylate (PEGDA)/CHW LC ink system, which can be used to conveniently and effectively construct LC hydrogel scaffolds with osteoid-like viscoelasticity, as demonstrated in Scheme 1. Furthermore, by adjusting the ratio of CHW to PEGDA, the modulus and LC state of the printed hydrogel scaffolds could be flexibly regulated. We hypothesized that viscoelasticity and LC state, typical characteristics of osteoid, can influence the behavior and osteogenic differentiation of BMSCs in a 3D environment, as well as regulate osteogenesis *in vivo*. To verify this hypothesis, we fabricated viscoelastic hydrogel scaffolds with varying modulus and LC states. We then explored how viscoelasticity and LC state impact BMSCs behavior and fate by analyzing the individual or synergistic effects of mechanical cues and protein clustering mediated by LC state in guiding BMSCs behavior *in vitro* and osteogenesis *in vivo*.
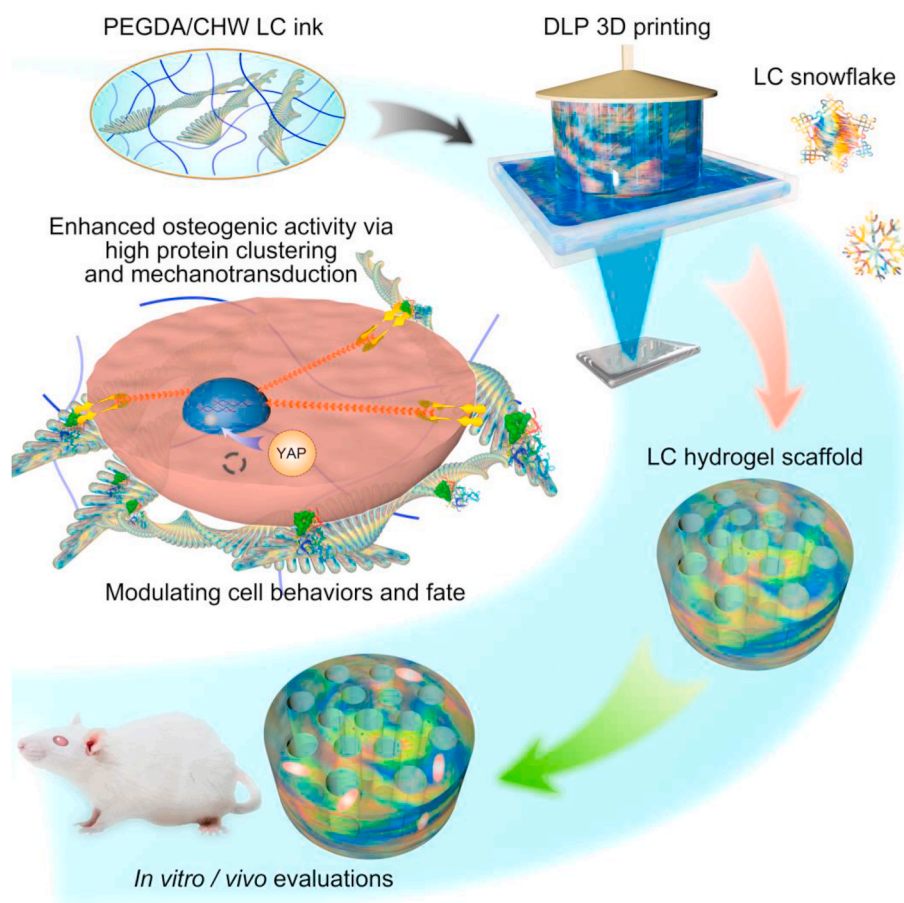
Scheme 1. Illustration of DLP printing of bioinspired LC hydrogel scaffolds with high protein clustering and tunable mechanotransduction based on a new type of PEGDA/CHW LC ink and *in vitro/in vivo* evaluations.

Our study provides theoretical guidance and broadens the research horizon for the design of biomimetic bone tissue engineering scaffolds.

2. Materials and methods

2.1. Materials

The raw α-chitin was obtained from Aladdin Chemical Co., Ltd. (Shanghai, China). PEGDA (M_w = 1000) and LAP was provided from Shanghai Macklin Biochemical Co., Ltd. Ethanol, hydrochloric acid (HCl) and other reagents were of analytical grade and purchased from Guangzhou Chemical Reagent Factory.

2.2. 3D printing of LC hydrogel scaffolds

Firstly, 10 wt% CHW LC suspension was prepared, and the detailed process has described in Supplementary information. Subsequently, mixed as-prepared CHW LC suspension and 20 wt% PEGDA aqueous solution, then added 0.2 wt% LAP as a photoinitiator to obtain printing precursor. Scaffolds with different modulus were obtained by adjusting the mass fraction of PEGDA added. For the preparation of nLC precursor, the 10 wt% CHW LC suspension was replaced with 10 wt% CHW suspension without LC state. Use DLP printer (SoonSer, China) with a wavelength of 405 nm to print and adjust parameters such as exposure time until a complete scaffold or a model is printed. The 3D printed samples were immersed in deionized water for 1 min, washed away the uncured precursor, and then solidified for 3–5 min under a 405 nm lamp.

2.3. Characterization of LC and mechanical properties

The LC texture of precursor and scaffolds was observed under a polarizing optical microscope (POM, BX53 M, Olympus, Tokyo, Japan) fitted with a digital camera (DP200). The circular dichroism (CD) signal was obtained through a circular dichroism spectrometer (Applied Photophysics Chirascan V100). The rheological properties of precursor and scaffolds were investigated through a rotary rheometer (TA Instruments, New Castle, DE, USA) at 25 °C. The viscoelasticity was tested at a strain of 0.5 % and a frequency range of 0.1–100 rad/s. The compressive properties were investigated by a universal testing machine (SHIMADZU, AG-1, Japan) with a rate of 2 mm/min at 25 °C. The mass swelling ratio was obtained by calculating the mass of the hydrogel after being soaked in PBS buffer solution for different times.

All modulus measurements via AFM method were performed at room temperature and used hemispherical dull probes from Bruker Instruments. A nanoscope controller and software versions 8.1 were utilized, and the DMT model was employed for a spherical indenter.

2.4. Mechano-chromic behaviors and finite element analysis

The mechano-chromic behaviors were investigated based on LC-HM hydrogels, and the size of samples used in bending test is 10 × 4 × 0.5 mm (length × height × width), the compression test sample is arch sample, and its semicircle diameter is 1.5 mm. The texture change of LC is recorded via POM. The finite element analysis of mechanical performances of scaffolds was carried out by Abaqus CAE (version 6.14). Finite element analysis is performed through the following steps: modeling, property definition, interaction, load setting (F = 100 N), tetrahedral meshing and visualization. The elastic modulus of the scaffold model was set to 10 kPa for low modulus scaffold and 100 kPa for high modulus scaffold, and the Poisson's ratio was set to 0.45.

2.5. Cell culture

Mouse BMSCs were obtained from Shanghai Bangjing Industry Co., Ltd. Dulbecco's modified eagle medium (DMEM, from Sperikon Life Science & Biotechnology co.,ltd), fetal bovine serum (FBS, from

Cellmax), antibiotics (Penicillin, Streptomycin) and trypsin-EDTA were used for cell culture. Cryotubes and other consumables were purchased from Promethe, Shanghai. Paraformaldehyde was purchased from Beijing Labgic Technology Co., Ltd. The viability of BMSCs was evaluated by live/dead fluorescent staining (APExBIO, Houston, USA). The proliferation of BMSCs was assessed via Cell Counting Kit-8 assay (CCK-8, Dojindo, Japan).

2.6. Cell morphology

The spreading behaviors of BMSCs were investigated via a laser scanning confocal microscope (LSCM) (Zeiss-LSM 510, Germany Carl Zeiss Jena). Cytoskeleton and nucleus were stained with rhodamine phalloidin and DAPI, respectively. After being dried by supercritical carbon dioxide, cell morphology was investigated by FESEM.

2.7. In vitro osteogenic activity

ALP activity was evaluated using AKP kit (Nanjing Jiancheng Bioengineering Institute). The type of collagen fibers secreted by cells was identified by Sirius staining (Solarbio, China). Calcium nodules were stained with 1 % alizarin red stain (Biosharp). Solution of dipotassium phosphate (24 mM) and calcium chloride (40 mM) was used for *in vitro* mineralization. Gene expression of cells cultured on various scaffolds was evaluated by real time PCR (RT-PCR, FongCyte, Challenbio). The primers sequences are summarized in Table S2. The RNase inhibitor is from East-Mab Bio (EB0108). The gene expression was calibrated to that of the housekeeping gene glyceraldehyde 3-phosphate dehydrogenase (GAPDH), and the data were determined by the comparative Ct ($2^{-\Delta\Delta Ct}$) method.

2.8. Immunofluorescence staining and inhibition assays

Vinculin polyclonal antibody (Cat No: 26520-1-AP) and Alexa Fluor 488 were employed to the vinculin immunostaining. The mean fluorescence intensity of vinculin was calculated by the Image J software. Rabbit polyclonal antibody (Cat No: E38A2479) and Alexa Fluor 488 were employed to the YAP immunostaining. The nucleus localization of YAP protein was determined by the Image J with a plugin of colocalization finder. The area ratio of YAP in nucleus was calculated as the intensity of the YAP signal within the nucleus divided by the intensity of the YAP signal outside of the nucleus in cytoskeleton area. The ML-7 (Med Chem Express, Shanghai) and Y-27632 (Med Chem Express, Shanghai) were added to the culture media for the inhibition of YAP and Rho, respectively.

2.9. Vitronectin (Vn) adsorption

The elemental compositions of Vn-adsorbed scaffolds with initial concentration of 10 μg mL^{-1} were investigated by X-ray photoelectron spectroscopy (XPS, Thermo, USA). The morphology of Vn-adsorbed scaffolds was visualized by AFM. Bicinchoninic Acid Assay (BCA) kit was used to detect the protein concentration of the supernatant after Vn adsorption. The functional capability of Vn adsorbed on scaffolds was revealed by human vitronectin enzyme-linked immunosorbent assay kit (EHVTN, Multi Sciences, Shanghai) using monoclonal antibodies specifically binding to the epitopes of the RGD-holding domains according to the manufacturer's instructions (n = 3). The structure of Vn was obtained from RCSB protein data bank (PDB: 1S4G and 2JQ8), and the electrostatic potential of protein was calculated by PyMol software.

2.10. Ectopic osteogenesis and skull repair evaluation

Ectopic osteogenesis: Male SD rats (Use permit: SYXK2020-0237, Ruige Biotechnology Co. Ltd) with an average weight of 200 g were used and randomly divided into 4 groups (n = 3). All procedures were

performed according to the approved guidelines of the local ethical committee for Animal Research (Approval No. IACUC HTSW220709). The rats were anesthetized and the hair on their backs was removed, and then 1 cm incisions were made on the left and right sides of the backs after disinfection. Finally, the sterilized scaffolds were implanted into the muscle chambers and sutured. The scaffolds were taken out according to the set time for observation and evaluation.

Skull repair evaluation: Healthy male SPF rats with an average weight of 200 g were used in this study (Use permit: SYXK 2023-0307, Bes Test Bio-Tech Co,.Ltd.) and randomly divided into 4 groups ($n =$ 3). All procedures were performed according to the approved guidelines of the local ethical committee for Animal Research (Approval No. IACUC B202310-13). After the animals were anesthetized, a 3 cm longitudinal incision was made in the skull to expose the bone plate. A high-speed drill with a 5 mm diameter was used to create a circular bony defect on both sides of the mid cranial suture of the skull. The scaffolds were then implanted, and the head wound was sutured. Finally, the rats were sacrificed at the 4 and 8 W and observed and stained for analysis.

The samples were scanned using SkyScan1276 to reconstruct the 3D model of bone defect, and three samples were analyzed at each time point. For morphological analysis, the samples were fixed in 10 % formalin for 5 days and decalcified in 15 % EDTA for 15 days, after which the samples were embedded in paraffin and cut into sections. These sections were stained with hematoxylin and eosin (HE) to assess general histology, and the Goldner's trichrome stain was employed to visualize tissue morphology and mineralization. Immunohistochemistry of COL-I and immunofluorescence staining of OCN were also performed. The **quantitative data of staining images is obtained via the Image J software, the H-score is calculated by the equal:**

$$H - score = \sum_{i=1}^{3} (1+i) * pi \tag{1}$$

where *i* is the intensity score and *pi* **is the percent of the cells with that intensity, and the percentage of cells with different grades of intensity is calculated by Image J** using the IHC Profiler plugin.

2.11. Statistical analysis

Statistical analysis was performed using Origin 2017 software. The quantitative results were exhibited as mean ± standard deviation, and One-Way ANOVA analysis of variance was employed to make the statistical analysis (*$p < 0.05$; **$p < 0.01$; ***$p < 0.001$).

3. Results and discussion

3.1. Viscoelastic and LC hydrogel scaffolds

The viscoelasticity of the hydrogels is primarily stemmed from the PEGDA crosslinking network, and hydrogels with different modulus
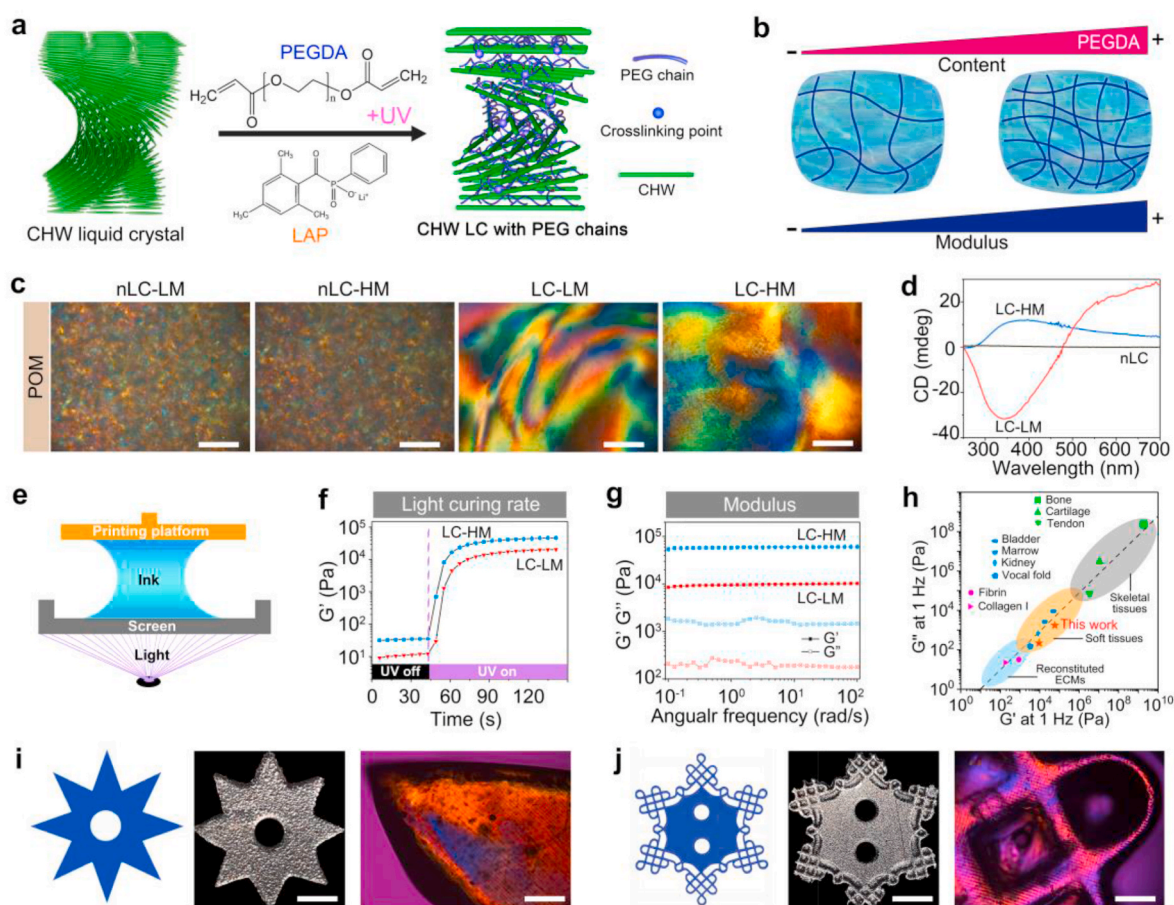

Fig. 1. a, b Schematic illustration of the preparation of LC hydrogels by introducing PEGDA chains into CHW helical structure. LC hydrogels with high and low modulus were obtained by adjusting the content of PEGDA. **c,** POM images of photo-crosslinked hydrogels with a color compensator. Scale bar is 400 μm **d,** CD spectra of hydrogels. The signal curves of nLC hydrogels including nLC-LM and nLC-HM groups almost overlap. **e,** Schematic diagram of main parts of DLP printer. **f,** The G′ of inks before and after UV irradiation (10 mW/cm²). The change of G′ was monitored by a rotational rheometer to reflect the photocuring rate of the inks. **g,** The G′ and G″ of hydrogels under frequency sweep tests. **h,** The plot of the G″ versus the G′ for the reconstituted ECMs and natural soft tissues according to other reports. The black dotted line presents the G″ that is 10 % of the G'. **i, j** Special-shaped parts printed based on the prepared LC-HM ink using DLP printing. From left to right are model, object (scale bar is 2 mm) and POM images (scale bar is 200 μm) of parts.

were achieved by finely adjusting the PEGDA content to modulate crosslinking density (Fig. 1a and b). Various printing inks were formulated, and their LC state and viscoelasticity were compared (Refer to Table S1). Typically, LC state of osteoid arises from the triple-helical structure of collagen fibers, exhibiting a cholesteric LC texture under polarized light and chirality. Insufficient PEGDA results in inadequate hydrogel curing, while excessive PEGDA disrupts the helical topology of the CHW LC. Consequently, PEGDA contents of 9.6 % and 8.0 % were

chosen for constructing high-modulus LC (LC-HM) and low-modulus LC (LC-LM) hydrogel scaffolds, respectively (Figs. S3–S5). Polarized light microscopy (POM) images of the LC-LM and LC-HM hydrogels display vibrant colors, indicative of a typical cholesteric LC texture (Fig. 1c). Similarly, LC state of collagen fibers in osteoid also exhibits a cholesteric LC texture. POM images of the non-liquid crystal (nLC) groups show no LC state, with only some CHW aggregates observed. Circular dichroism (CD) signals ranging from 300 to 700 nm appeared in the CD spectra of
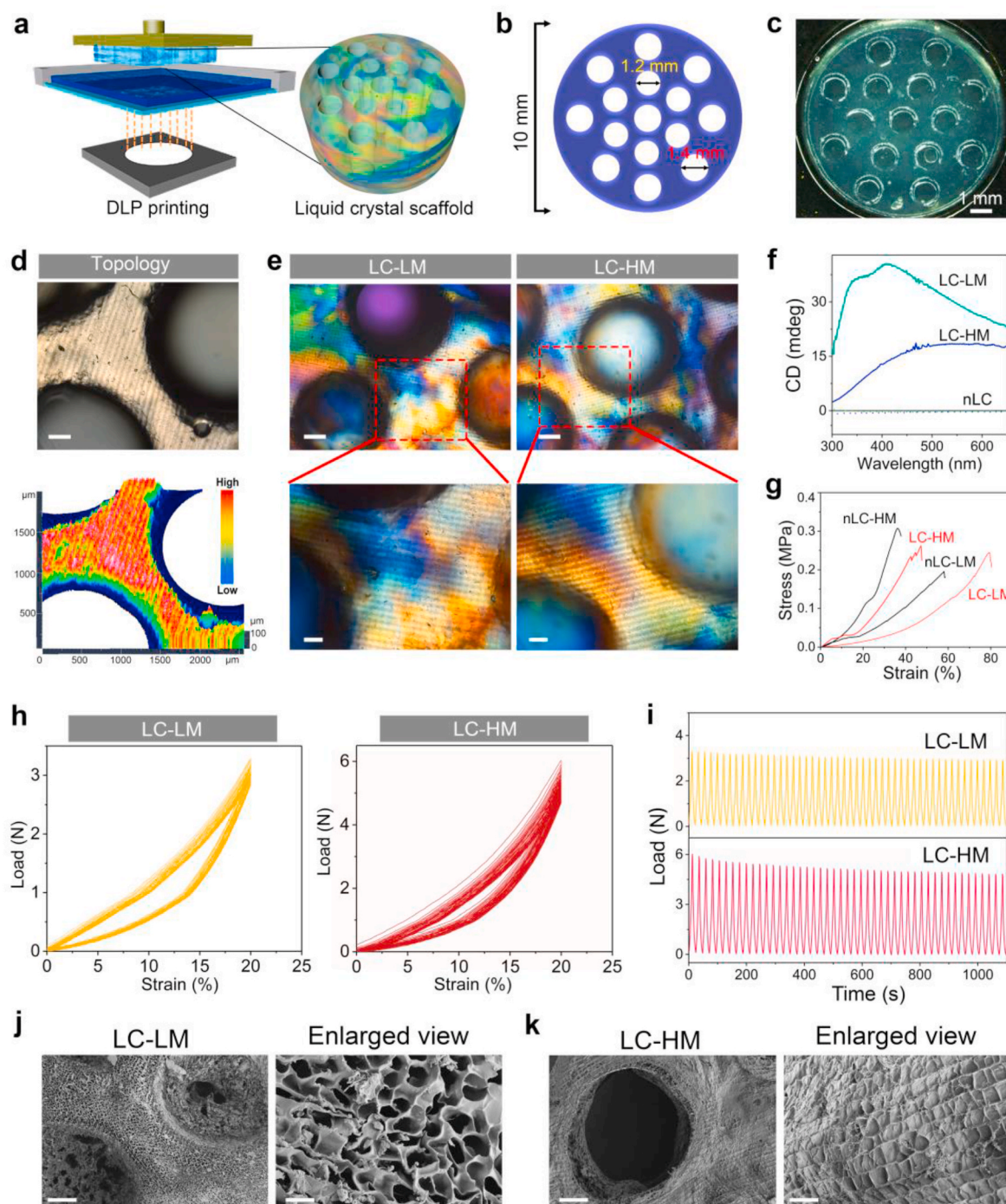
Fig. 2. a, Schematic diagram of the process of DLP printing and the LC hydrogel scaffold. b, Model diagram of LC hydrogel scaffold. c, Stereomicroscopy photograph of the LC hydrogel scaffold. Scale bar is 1 mm d, 3D images of the LC hydrogel scaffold taken according to the principle of depth-of-focus imaging. Scale bar is 200 µm. e, POM images (scale bar is 250 µm) and the enlarged view (scale bar is 100 µm) of LC-LM and LC-HM hydrogel scaffolds. f, CD spectra of hydrogel scaffolds. The signal curves of nLC scaffolds including nLC-LM and nLC-HM groups almost overlap. g, Compressive stress-strain curves of LC-LM and LC-HM hydrogel scaffolds. h, i, The cyclic compression and time-load curves of the LC-LM and LC-HM hydrogel scaffolds under 20 % strains (50 cycles). j, k, The FESEM images (scale bar is 200 µm) of LC-LM and LC-HM scaffolds and their enlarged view (scale bar is 20 µm).

the LC-HM and LC-LM hydrogels, confirming the presence of a chiral topology in the hydrogels (Fig. 1d). Although the CD spectrum of the LC-LM hydrogel displays two types of chiral signals, the left-handed signal (positive signal) predominates, suggesting that PEGDA chains do not disrupt the left-handed helical structure of the CHW LC. The absorbance spectra corresponding to the CD spectra are illustrated in Fig. S6. These findings demonstrate that the photocrosslinked hydrogels effectively maintain LC state of CHW.

Before printing the hydrogel scaffolds, adjustments were made to the printability of the LC ink to ensure the structural accuracy of the scaffolds. The rheological properties of the LC ink during the printing process are crucial (Fig. 1e), as they determine the curing time and printing speed of each layer. Real-time monitoring of the crosslinking rate was conducted by observing the storage modulus (G′) with a rheometer while applying UV light to the ink, as depicted in Fig. 1f. Although the LC-HM ink exhibits a slightly faster crosslinking rate compared to the LC-LM ink, both LC inks complete crosslinking within 20 s, indicating efficient photo-crosslinking performance. The modulus of the cured LC-HM hydrogel was approximately 72.3 kPa, while that of the LC-LM hydrogel was approximately 12.3 kPa. Additionally, the inks displayed suitable viscosities and thermal stability (Figs. S7 and S8). Further investigation of the mechanical properties of the hydrogels was conducted through frequency sweeping, providing insights into the viscoelasticity of the as-prepared LC hydrogels. The results clearly demonstrate elastic behavior in the LC hydrogels (G′ > G″, where G″ represents the loss modulus), attributed to the presence of both covalent and hydrogen bonds (Fig. 1g). The fate of BMSCs is linked to the modulus, with BMSCs differentiating towards osteogenesis when G′ exceeds 9–17 kPa [2–4,19]. In this study, the G′ of the LC-HM and LC-LM groups ranged from 50 to 70 kPa and 8–10 kPa, respectively. Furthermore, the ratio of G″ to G′ of the LC hydrogels was approximately 10 %, similar to that of reconstituted ECMs and natural soft tissues (Fig. 1h). The nLC hydrogels also fell within the range of modulus settings (Fig. S9). To further assess the printing performance of the selected LC ink, printing tests of special-shaped parts such as octagons and "snowflakes" were conducted using DLP printing (Fig. 1i and j). The printed parts closely resembled the models, with LC state well-preserved (Fig. S10), confirming the excellent printability of the LC ink.

After acquiring inks capable of forming osteoid-like hydrogels, LC hydrogel scaffolds with varying modulus were fabricated using DLP printing (Fig. 2a). The scaffolds were designed to be 10 mm in diameter, with outer and central holes measuring 1.4 mm in diameter, and an inner hole measuring 1.2 mm in diameter (Fig. 2b). The printed scaffolds closely matched the model in terms of size (Fig. 2c), and the scaffolds with different sizes were also depicted in Fig. S11. Optical microscopy revealed the topographic structure of the scaffold (Fig. 2d), where the light path from DLP printing was observed to be preserved on the LC hydrogel scaffolds at a size of 20–50 μm. Notably, micron-scale topological structure [20–22], as derived from the printing process, have been found to potentially enhance cell adhesion and migration, thus offering an advantage for bone regeneration. The LC texture of the as-printed hydrogel scaffolds was observed (Fig. 2e). Both LC-LM and LC-HM hydrogel scaffolds exhibited a distinct LC texture, which was absent in the nLC groups (Fig. S12). Additionally, CD signals of the LC-LM and LC-HM groups were evident in the CD spectra compared to those of the nLC groups (Fig. 2f), suggesting a typical chiral topological structure in the printed LC hydrogel scaffolds. Corresponding absorbance spectra are provided in Fig. S13. Interestingly, differences in CD signals between the printed scaffolds and corresponding hydrogels were noted, possibly due to interference in chirality caused by the scaffold's topological structure. These findings affirmed that DLP-printed scaffolds retained the osteoid-like chiral LC state. The compressive properties of the hydrogel scaffolds are depicted in Fig. 2g, revealing a certain level of toughness with a maximum fracture strain of 78.7 %. Elasticity of the hydrogel scaffolds was further assessed through compression cycle experiments (Fig. 2h and i). After 50 cycles of compression, a slight decrease in the strength of the hydrogel scaffolds was observed, indicating relatively stable mechanical and elastic properties. Morphological analysis of the hydrogel scaffolds using FESEM revealed distinct surface characteristics (Fig. 2j and k, and S14). The high-modulus scaffold displayed a tight network on its surface, while pores on the surface of the low-modulus scaffold appeared relatively loose, elucidating differences in mechanical properties among the scaffolds.

As the constructed scaffolds have a porous structure, leading to variations in the modulus distribution of the 3D scaffolds, it becomes necessary to detect the point modulus of the scaffolds. While the modulus range of bulk hydrogels can be determined using a rheometer, it is not suitable for detecting the distribution of point modulus on scaffolds. PeakForce Tapping by atomic force microscopy (AFM) was employed to investigate the point modulus of the hydrogel scaffolds in a PBS buffer solution (Fig. 3a). The force-separation curves depicted in Fig. 3b are divided into two stages: linear compression and probe retraction. To further discern the difference in point modulus among the printed scaffolds, the retraction of different scaffolds was analyzed (Fig. 3c). It was observed that low-modulus hydrogel scaffolds exhibited a larger maximum deformation compared to high-modulus scaffolds. A larger maximum deformation indicates a softer scaffold. Moreover, the point modulus on the high-modulus scaffolds ranged from 39.1 to 118 kPa, while on the low-modulus scaffolds, it ranged from 3.4 to 14.2 kPa (Fig. 3d). This outcome suggests a significant difference in modulus among the printed scaffolds, aligning with our hypothesis. Additionally, differences in modulus were observed at various sites on the same scaffold. According to finite element analysis, the modulus outside the scaffold (zone I) exceeded that inside (zone II), as illustrated in Fig. 3e and f. This discrepancy may be attributed to more pores on the inner side of the scaffolds undergoing larger deformation, resulting in a lower modulus under the same force.

The optical properties of cholesteric LC stem from the helical topology of CHW; thus, we hypothesize that LC hydrogels exhibit a robust mechanochromic response due to changes in the pitch of the helical topology (Fig. 3g). To verify this, a bending test was conducted on the printed LC hydrogel. As depicted in Fig. 3h and i, the polarizing color transitioned from orange to blue-green when the LC hydrogel was bent. Notably, the most pronounced color shift occurred on both sides of the LC hydrogel. Through finite element analysis, it was observed that larger deformation occurred on these sides, resulting in a greater change in the pitch of the LC and a more significant color shift. Subsequently, a hydrogel model (Fig. 3j) was designed to demonstrate the intelligent chromic response of the hydrogels to regions of stress concentration. Upon applying pressure to the arched hydrogel, it was observed that the region with the most noticeable color shift corresponded with the region of stress concentration identified in the finite element analysis (Fig. 3k). This observation supports our hypothesis that LC hydrogels can indicate stress concentration through changes in the LC topology, which could be exploited in the design of mechano-optical sensors.

3.2. Cell behaviors and fate in viscoelastic and LC hydrogel scaffolds

The cell affinity of the scaffolds was assessed through live-death and proliferation assays (Figs. S15 and S16), revealing excellent cell affinity across all scaffolds. Analysis of 3D LSCM images (Fig. 4a) indicated even distribution of cells throughout the scaffolds after 72 h of culture. Notably, the cell density on high-modulus scaffolds exceeded that on low-modulus scaffolds. Height scanning of the scaffolds unveiled cell growth within the pores, further confirming the favorable cell affinity of the hydrogel scaffolds. Subsequent observation of cell spreading morphology on the scaffolds, along with quantification of cell spreading area, revealed differences among the groups (Fig. 4b and c). After 36 h of culture, cells on high-modulus scaffolds exhibited larger spreading areas and more pronounced actin filaments compared to those on low-modulus scaffolds, suggesting a greater inclination of cells to adhere to high-modulus scaffolds. SEM images (Fig. 4d) confirmed this
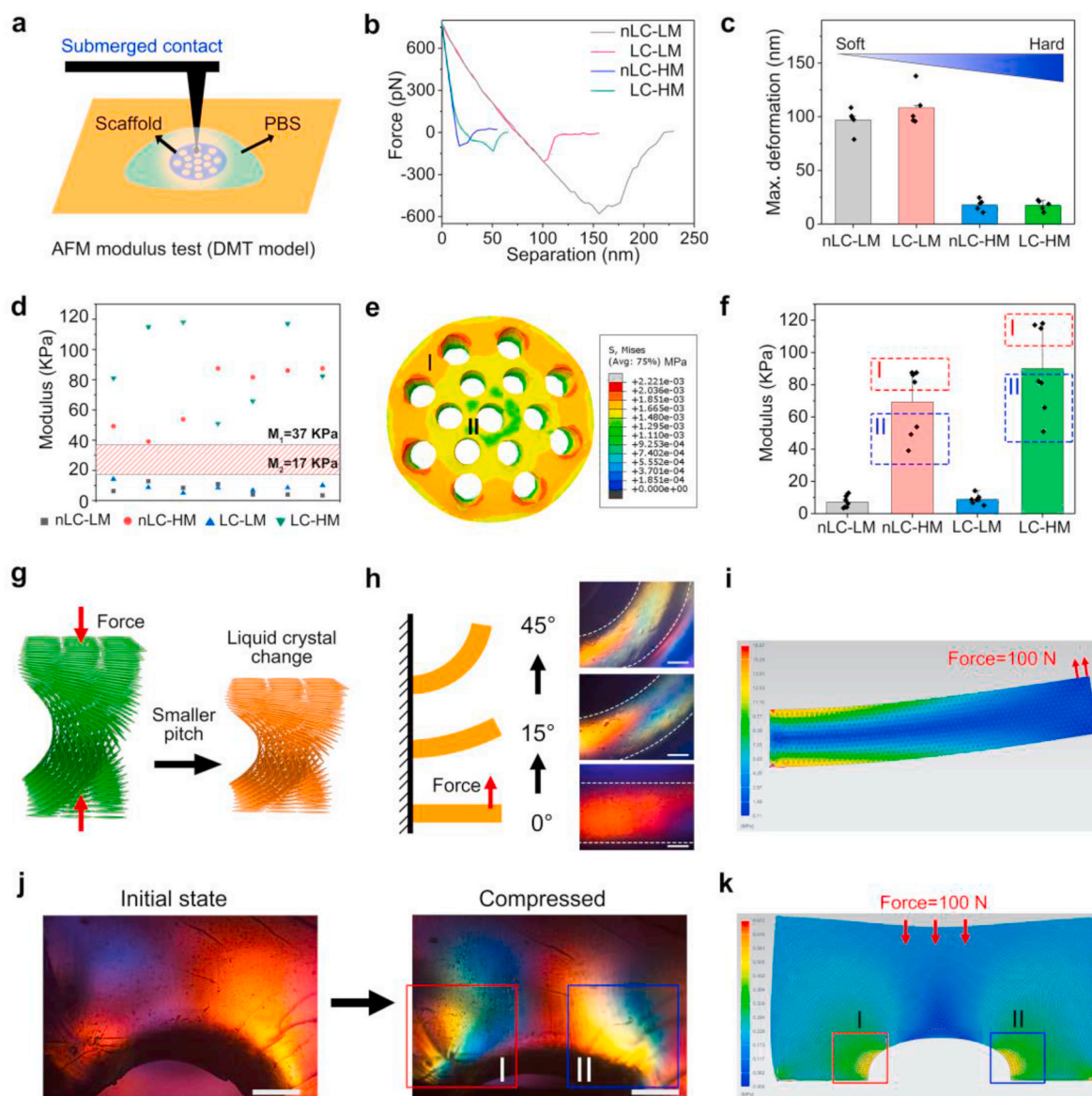
Fig. 3. a, Schematic illustration of measuring the modulus at different positions of the hydrogel scaffolds in underwater environment. **b,** The curves of the deformation and force of the hydrogel scaffolds. **c,** Histogram of maximum deformation for different hydrogel scaffolds. ($n = 5$) **d,** Modulus of different hydrogel scaffolds calculated by the Derjaguin-Müller-Toporov (DMT) fit. ($n = 7$) **e-f,** Finite element analysis of the hydrogel scaffolds when it was loaded and the histogram of modulus of scaffolds. ($n = 7$) Regions I and II represent high and low stress regions, respectively. **g,** Schematic illustration of change of the pitch of LC hydrogels after being compressed. **h-i,** Mechano-chromic behavior and finite element analysis of LC hydrogels during bending. Scale bar is 0.25 mm. **j-k,** Mechano-chromic behavior and finite element analysis of LC hydrogels during compression. Scale bar is 0.25 mm.

observation, with high-modulus scaffolds displaying larger cell spreading areas than low-modulus scaffolds. Moreover, various cell responses on the scaffolds were observed in the enlarged views of the SEM images. Cells on low-modulus scaffolds exhibited short pseudopodia, while those on high-modulus scaffolds displayed longer pseudopodia and appeared more stretched, indicating the beneficial effect of high-modulus scaffolds on promoting cell adhesion and spreading. To statistically validate the effect of modulus on cells, cell morphology was analyzed after 12 h of scaffold culture (Fig. 4e). Cell polarity, defined as the ratio of the major axis to the minor axis of cells, was used as a measure of cell spreading state. Cells with a polarity closer to 1 exhibited a rounder shape, while those with a higher polarity demonstrated morphological polarization. As illustrated in Fig. 4f, cells on low-modulus scaffolds mainly exhibited polarities in the range of 1–2, indicating a non-spreading state, whereas those on high-modulus scaffolds displayed larger polarities, indicative of favorable spreading

behavior. The proportions of cells with different polarities are depicted in Fig. 4g, showing a higher proportion of polarized cells in the high-modulus group compared to the low-modulus group, underscoring the superior cell adhesion, spreading, and migration facilitated by high-modulus scaffolds. These findings underscore the pivotal role of scaffold modulus in regulating cell morphology and spreading, primarily through the feedback of polymer chains to cell mechanics [3,23–25]. A tighter network provides strong adhesion points for cell pseudopodia, thereby promoting cell spreading and migration, whereas a looser network may impede cell anchoring after contacting the scaffolds (Fig. 4h). Additionally, a greater number of polarized cells on LC-HM scaffolds compared to nLC-HM scaffolds suggests an influence of LC state on cell adhesion and spreading behaviors, possibly attributed to increased protein adsorption by LC state in early stages, subsequently enhancing cell spreading. This hypothesis is further validated.

Alkaline phosphatase (ALP) secretion serves as an early indicator of
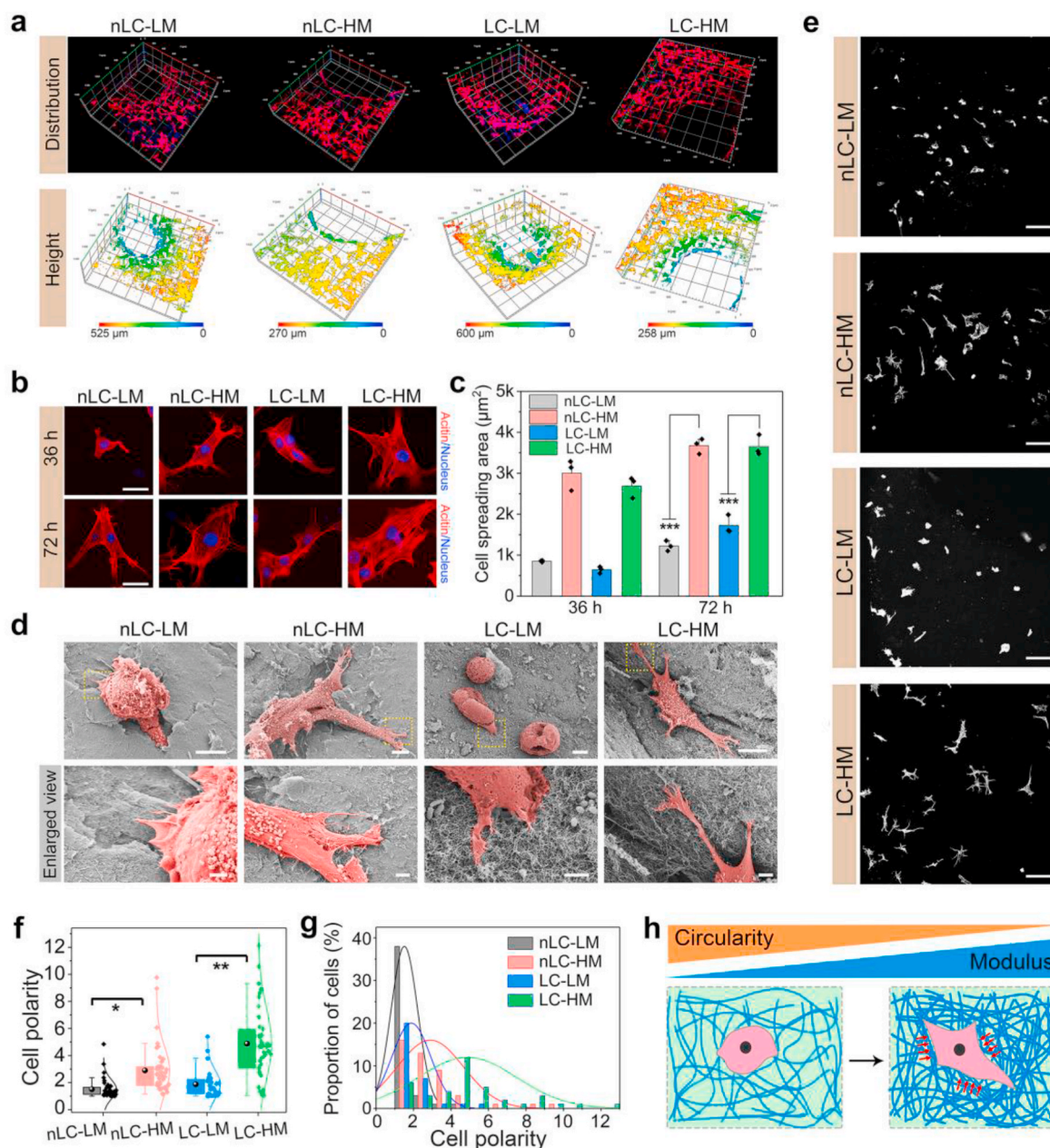
Fig. 4. a, 3D LSCM and height images of BMSCs cultured for 72 h on hydrogel scaffolds. **b, c,** 2D LSCM images and cell spreading area of BMSCs cultured for 36 and 72 h on hydrogel scaffolds, respectively. Scale bar is 30 μm. (***$P < 0.001$, ANOVA) **d,** SEM images of BMSCs on hydrogel scaffolds and their enlarged view, where the color of SEM images is artificially added to distinguish cells from scaffolds. Top scale bar is 10 μm, and bottom scale bar is 2 μm. **e,** Cells after culturing for 12 h were imaged using LSCM and cell outlines were shaped. Scale bar is 70 μm. **f,** Cell polarity was calculated for cells shape on different hydrogel scaffolds. (*$P < 0.05$, **$P < 0.01$, ANOVA, $n = 30$) **g,** Statistics on the proportion of cells with different polarity. ($n = 30$). Data in **f** and **g** were obtained by tracing the cell shape in **e** via Fiji software. **h,** Schematic illustration of cell spreading on hydrogel scaffolds with different modulus.

BMSCs' osteogenic differentiation ability on scaffolds; hence, ALP secretion was monitored. At 7 d, ALP secretion (depicted by black particles) was observed in all scaffolds (Fig. 5a). Notably, the LC-HM scaffold exhibited the most obvious ALP secretion compared to other scaffolds, a point confirmed by quantitative analysis of ALP in Fig. 5b. By day 14, a more significant difference in the osteogenic properties of the scaffolds began to emerge. All high-modulus scaffolds exhibited higher ALP secretion than low-modulus scaffolds, highlighting the osteogenic promotion effect of the high-modulus environment. Importantly, the LC-HM scaffold displayed the highest osteogenic activity, markedly differing from that of the nLC-HM scaffold. This underscores the crucial role of LC state in promoting early osteogenic differentiation of BMSCs, particularly in a high-modulus environment, indicating a synergistic

effect between LC state and high modulus in promoting osteogenic differentiation, thus preliminarily confirming our hypothesis. Type I collagen (COL-I), a significant indicator of osteogenic differentiation, is secreted by osteoblasts to build osteoid. Sirius Red specifically stains COL-I, rendering it bright red under POM. Compared to low-modulus scaffolds, high-modulus scaffolds exhibited a larger positive red area, with LC-HM scaffolds displaying the largest positive area (Fig. 5c). This suggests that LC state and high-modulus environment of the LC-HM scaffold also significantly promote the secretion of COL-I. Furthermore, late osteogenic activity of the scaffolds was investigated using an alizarin red assay. As illustrated in Fig. 5d, after 21 d of culture, conspicuous calcium deposition was observed on scaffold surfaces. More calcium deposits were observed on high-modulus scaffolds compared to
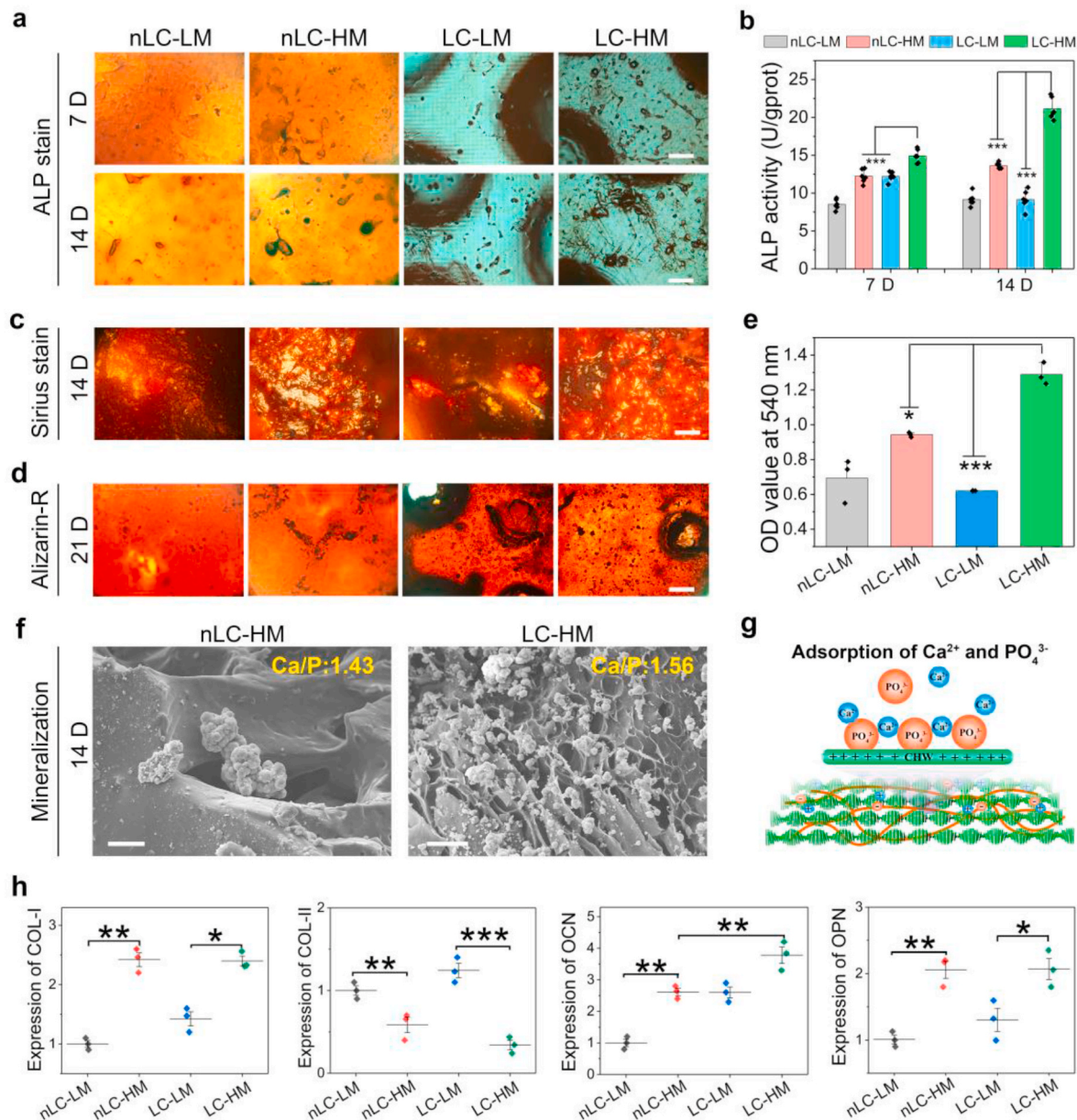
Fig. 5. a, The ALP staining images of BMSCs after culturing for 7 and 14 d on scaffolds. The color difference of images between the nLC and LC groups is due to the difference in the light transmittance. The nLC scaffolds with the poor light transmission use the transmission mode to take images, while the LC scaffolds use the reflection mode. Scale bar is 150 μm **b,** The ALP activity of BMSCs after culturing for 7 and 14 d on hydrogel scaffolds. (***$P < 0.001$, ANOVA, $n = 5$) **c,** POM images of the Sirius stain, where bright red is the positive area. Scale bar is 150 μm **d,** Alizarin red staining of cells cultured on scaffolds for 21 d. Scale bar is 150 μm. **e,** Quantitative analysis of alizarin red staining of cells cultured on hydrogel scaffolds for 21 d (*$P < 0.05$, ***$P < 0.001$, ANOVA, $n = 3$) **f-g,** The FESEM images of nLC-HM and LC-HM scaffolds after 14 d of *in vitro* mineralization, and the diagram of the potential mechanism of the LC-HM scaffold mineralization. The ratio of Ca/P of mineralization was calculated by the energy dispersive spectroscopy (EDS) scanning. Scale bar is 30 μm **h,** Quantitative analysis of the gene expression of COL-I, COL-II, OCN and OPN of cells cultured on scaffolds for 7 d (*$P < 0.05$, **$P < 0.01$, ***$P < 0.001$, ANOVA, **n=5).**

low-modulus scaffolds. Additionally, quantitative analysis of alizarin red stain revealed a positive synergistic role of LC state and high modulus environment in calcium deposits (Fig. 5e). Previous studies have demonstrated that 2D LC hydrogel membranes can promote mineralization [18,26]. Therefore, we attempted to replicate this result on 3D LC hydrogel scaffolds. As depicted in Fig. 5f and g, a higher deposition density was observed on the LC-HM scaffold than on the nLC-HM scaffold. Moreover, the calcium-to-phosphorus ratio of the deposits on the LC-HM scaffold was closer to the calcium-to-phosphorus ratio of natural bone, indicating the osteoid-like LC state of the hydrogel scaffolds serves as an ideal template for calcium phosphate deposition and mineralization.

The effects of the modulus and LC state of the hydrogel scaffolds on the osteogenic differentiation of BMSCs were examined through genetic analysis. COL-I and type II collagen (COL-II) are genes associated with osteogenesis and chondrogenic differentiation [27–30], respectively. As expected, the high-modulus groups exhibited higher COL-I expression, while the low-modulus groups showed higher COL-II expression (Fig. 5h). This suggests that high-modulus scaffolds are more conducive to osteogenic differentiation, whereas low-modulus scaffolds promote chondrogenic differentiation of BMSCs. Additionally, osteocalcin (OCN) and osteopontin (OPN), important markers of osteogenic differentiation in BMSCs [31,32], were further monitored by RT-PCR. We found that high-modulus scaffolds exhibited higher OCN and OPN expression than

low-modulus scaffolds. More importantly, high-modulus scaffolds in LC state showed higher expression compared to nLC-HM scaffolds, consistent with the results of the ALP and alizarin red assays. These findings support the hypothesis that LC state and mechanical microenvironment of hydrogel scaffolds significantly regulate the behavior and fate of BMSCs.

3.3. Mechanisms of mechanotransduction and protein clustering

Given that differences in the modulus among scaffolds may result in varying levels of vinculin expression, we investigated vinculin expression in cells to determine whether vinculin plays a role in mechanically induced osteogenic differentiation [33–35]. As shown in Fig. 6a, cells on
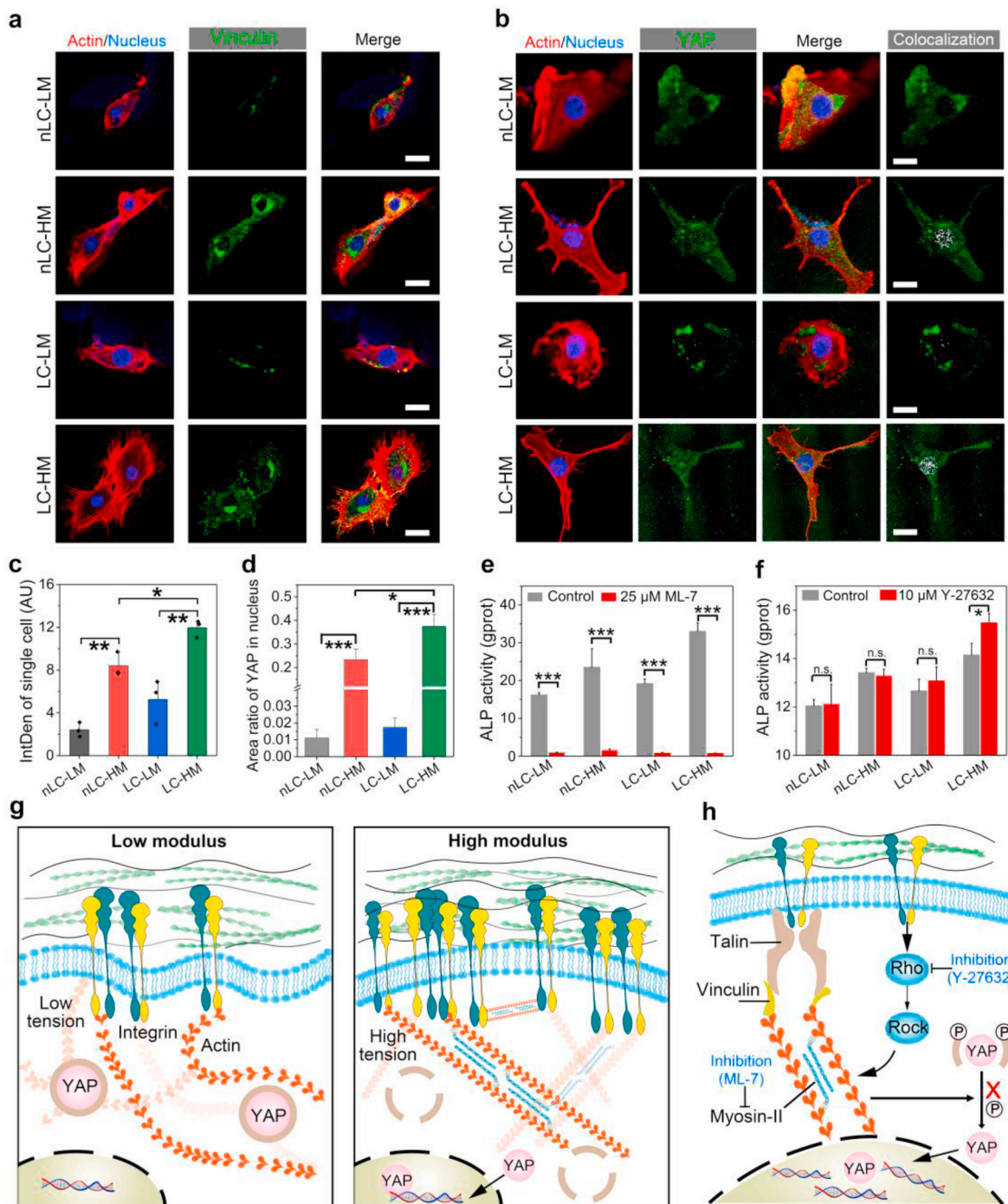
Fig. 6. a, LSCM images and merge images of actin (red), nucleus (blue), and vinculin (green) of cells on hydrogel scaffolds after 36 h of culture. Scale bar is 20 μm **b,** LSCM images and merge images of actin, nucleus, and YAP (green) of cells cultured on hydrogel scaffolds for 36 h. The colocalization images of YAP and nucleus, where the YAP in nucleus is identified in white. Scale bar is 20 μm. **c,** Fluorescence IntDen of vinculin of single cell. The density of vinculin was analyzed by Fiji software. (*$P < 0.05$, **$P < 0.01$, ANOVA, $n = 3$) **d,** Quantitative analysis of the area proportion of YAP in nucleus (*$P < 0.05$, ***$P < 0.001$, ANOVA, $n = 3$) **e, f** ALP activity before and after inhibition by ML-7 (a myosin light chain kinase inhibitor) and Y-27632 (a Rho kinase inhibitor), respectively. The control groups are the scaffolds without inhibitors. (*$P < 0.05$, ***$P < 0.001$, n. s. means no significant difference between groups. ANOVA, $n = 3$) **g,** Schematic illustration of the effect of viscoelasticity and LC state on the cytoskeleton and the distribution of YAP in the nucleus. **h,** Potential osteogenic signaling pathways revealed by inhibition assays. P indicates the phosphorylated YAP.

the high-modulus scaffolds exhibited an obvious vinculin-positive area, whereas those on the low-modulus scaffolds showed very limited vinculin expression. This indicates that high-modulus scaffolds promote the formation of focal adhesions, thereby regulating cell adhesion, and confirms that the scaffold modulus plays a key role in this process. Through quantitative analysis of vinculin (Fig. 6c), we found that the fluorescence integrated density (IntDen) of vinculin in single cells on the LC-HM scaffold was significantly higher than that on the nLC-HM scaffold, with a statistically significant difference. This result suggests that LC state enhances the formation of focal adhesions, and more importantly, this positive effect is significantly amplified by the synergistic effect of the scaffold's viscoelasticity. Yes-associated protein (YAP) is a downstream transcription factor of the Hippo signaling pathway, serving as a major sensor of cellular physical properties and being highly related to cell mechanics, structure, and polarity [36,37]. YAP can enter the nucleus through dephosphorylation and induce osteogenic differentiation of BMSCs. Therefore, we monitored the colocalization of YAP with the nucleus (Fig. 6b). YAP in cells on low-modulus scaffolds was mainly concentrated in the cytoplasm, whereas on high-modulus scaffolds, more YAP was observed in the nucleus. This finding reveals that the nuclear transfer of YAP is an important process by which the scaffold modulus regulates the osteogenic differentiation of BMSCs. Furthermore, through quantitative analysis of YAP-nucleus colocalization (Fig. 6d), we found that the LC-HM scaffold had the highest level of YAP-nucleus colocalization, indicating that LC state also plays a significant positive role in promoting the osteogenic differentiation of BMSCs by activating YAP.

YAP is regulated by cellular tension, and the cytoskeleton, composed of actin, depends mainly on the ECM environment. When cells are seeded on high-modulus scaffolds, they tend to form distinct focal adhesions and increase intracellular tension. Myosin II chains, important structures in cellular transport mechanics, can alter nuclear pore size to induce YAP entry (Fig. 6g). It is worth noting that the Rho signaling pathway is the main pathway through which cells perceive the ECM, suggesting potential crosstalk between the Hippo/YAP and Rho/ROCK signaling pathways [38,39]. Therefore, we conducted pharmacological inhibition experiments on myosin II and Rho kinase to determine their roles in the nuclear transfer of YAP. We monitored ALP expression in different groups. After inhibiting myosin II in BMSCs with ML-7, ALP expression decreased significantly in all scaffolds (Fig. 6e), revealing that the osteogenic activity of the LC-HM scaffold is closely related to myosin II in BMSCs. After inhibiting Rho kinase, we found no significant change in the osteogenic activity of most scaffolds, except for an increase in the osteogenic activity of the LC-HM scaffold (Fig. 6f). This indicates that there is no crosstalk between the Rho/ROCK and Hippo/YAP signaling pathways. Overall, these results indicate that YAP plays a key role in inducing osteogenic differentiation of BMSCs on the LC-HM scaffold. BMSCs in LC state and high-modulus environment exhibit enhanced focal adhesion, improving intracellular tension dominated by myosin II (Fig. 6h). This increased tension promotes the nuclear transfer of YAP, leading to high osteogenic activity of the LC-HM scaffold.

In summary, the results revealed that the viscoelasticity of the LC hydrogel scaffolds promotes the osteogenic differentiation of BMSCs through YAP-dependent mechanotransduction, and that LC state further enhances this promotion. It is also worth mentioning that the YAP-dependent mechanotransduction of LC hydrogel scaffolds on the osteogenic differentiation of BMSCs can be adjusted by controlling the modulus of the LC hydrogel scaffolds.

As mentioned above, LC state of the hydrogel scaffolds plays a significant role in the regulation of cell adhesion and osteogenic differentiation. However, the manner in which LC state affects cells has always puzzled us. Various proteins are present in osteoid, such as Vn and fibronectin (Fn), which can regulate BMSCs adhesion, proliferation, and differentiation [40,41]. Hence, investigating the interaction between proteins and scaffolds may help elucidate the mechanism by which LC

state affects cell behaviors and fate. In this study, Vn was chosen to investigate cell–scaffold interactions. We observed the morphology of Vn adsorbed onto the scaffolds using AFM. The spherical protrusions on the surface of the scaffolds were considered clusters formed after Vn adsorption (Fig. 7a). Compared to the nLC-HM scaffold, the LC-HM scaffold showed more spherical protrusions and greater roughness, implying that LC state is beneficial for protein clustering. Furthermore, according to the profile curves of the height images, we found that the projected area of the Vn clusters on the nLC-HM scaffold was smaller than that on the LC-HM scaffold. The larger the projected area of Vn on the scaffold, the greater the chance for cells to combine with Vn. We further examined the nitrogen content of the scaffolds before and after Vn adsorption (Fig. 7b). The N 1s peak on the surface of the scaffolds was significantly higher after adsorption, and the intensity of the LC scaffolds was higher than that of the nLC scaffolds, indicating higher protein clustering on the LC scaffolds. Additionally, we detected Vn in the supernatant after adsorption (Fig. 7c). Compared to the nLC scaffolds, the supernatant of the LC scaffold group had a lower Vn concentration, indicating that the LC scaffolds adsorbed more Vn. Notably, high protein density is not equivalent to good cell adhesion and osteogenic activity. The Arg-Gly-Asp (RGD) motif, as the key cell-binding site, is commonly regarded as the functional segment of Vn and determines cell response to Vn by activating integrin receptors on the cell membrane, such as αvβ1 and αvβ5 [34,42]. Hence, the exposure of RGD is critical for the regulation of cell behaviors and fate. The amount of exposed RGD on the scaffolds was detected by ELISA (Fig. 7d), indicating that the exposed RGD motifs on the LC scaffolds were greater than those on the nLC scaffolds. Altogether, both qualitative and quantitative results indicated that LC state of the scaffolds significantly enhances Vn protein clustering.

The adsorption amount of Vn and exposure of RGD are related to the structure of Vn on the scaffold surface, which is determined by the surface properties of the scaffolds. Somatomedin B (SMB), a functional domain of Vn containing RGD motifs, was used to study the interaction between Vn and the scaffolds. We selected three common SMB structures, whose configurations and potential distributions are shown in Fig. 7e. The potential at the RGD terminal (green) was approximately zero, while the opposite side of the RGD terminal had a distinctly negative potential (red). We speculated that this potential distribution might favor the adsorption of the SMB domain of Vn and the exposure of the RGD motif on the LC hydrogel scaffolds (Fig. 7f). CHW is positively charged due to amino groups, which can affect the adsorption morphology of SMB, and in turn, the exposure of the RGD terminal. Owing to electrostatic interactions, the negative potential region of Vn combines with CHW, attracting more Vn and exposing the RGD motifs. In contrast, the Vn aggregates formed in the fixed topology of the LC scaffolds were more stable compared to the disordered CHW topology of the nLC scaffolds. Additionally, subsequent Vn formed clusters with the adsorbed Vn due to hydrophobic interactions. Furthermore, although both the LC-LM and LC-HM scaffolds had more Vn clusters, they differed significantly in terms of cell fate. This indicates that Vn is not the sole determinant of cell fate. Adsorbed Vn clusters may act as amplifiers of mechanotransduction, with high-density Vn activating more integrins, making BMSCs more sensitive to the high-modulus scaffold and thereby improving osteogenic differentiation (Fig. 7g). However, for the LC-LM scaffold, the amplified low-modulus cue limited the osteogenic differentiation of the BMSCs. The mechanism of protein clustering explains the difference in Vn adsorption capacity between the LC and nLC scaffolds.

3.4. Viscoelastic and LC hydrogel scaffolds assist bone repair

Given that the viscoelasticity and LC state of the hydrogel scaffolds play a synergistic role in guiding the osteogenic differentiation of BMSCs *in vitro*, we further investigated whether this effect also promotes bone formation *in vivo* (Fig. 8a). We recorded the morphological changes in
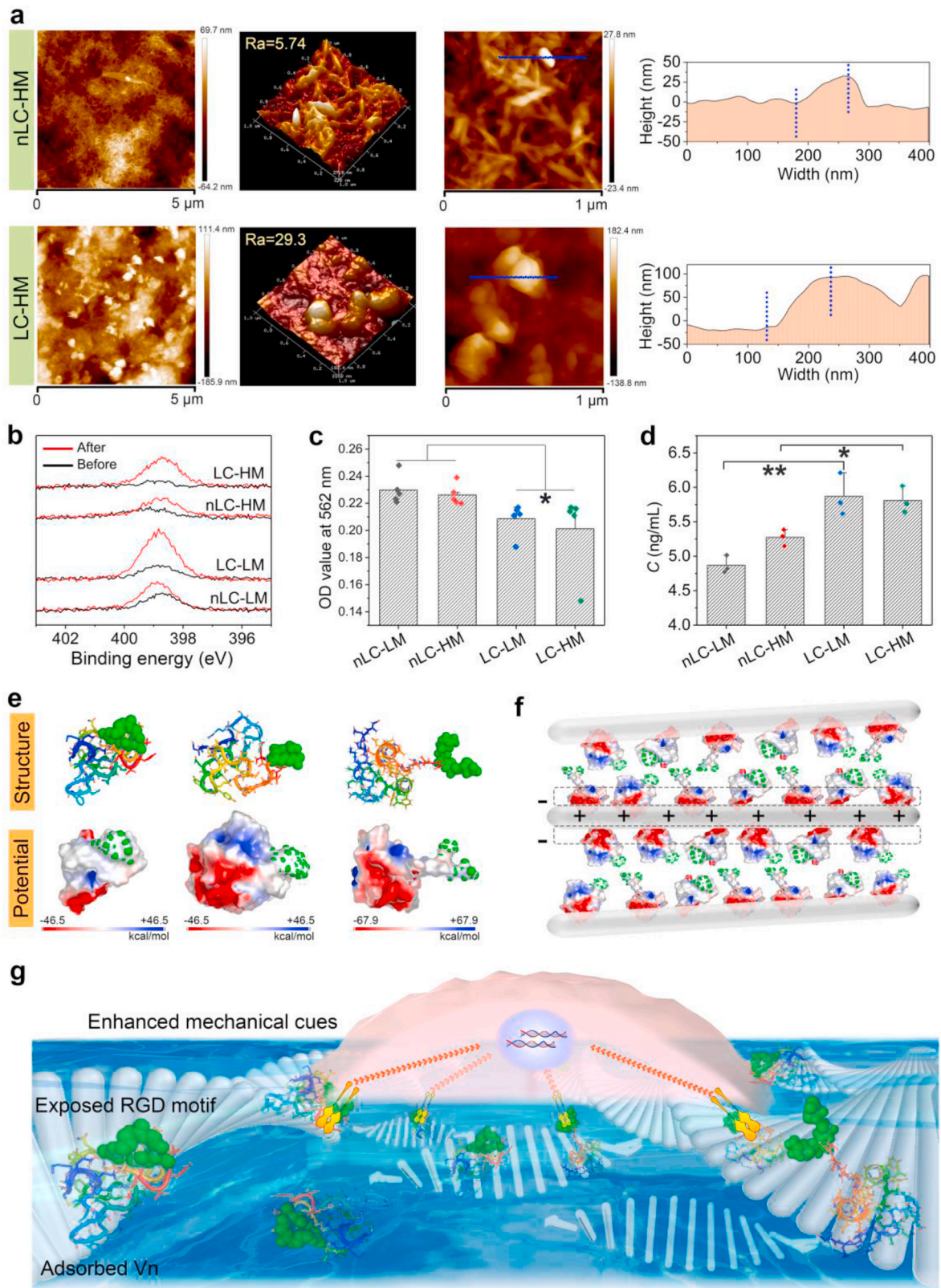
Fig. 7. a, The height, 3D AFM images and profiles of the hydrogel scaffolds before and after Vn adsorption. **b,** The N 1s peaks of the scaffolds before and after the protein adsorption. **c,** OD value of Vn in supernatants after adsorption by different scaffolds. ($n = 5$) **d,** Amount of RGD exposed of Vn clusters measured by ELISA. ($n = 3$) **e,** Structure and potential distribution of SMB obtained by PyMol. The RGD motif is marked in green. **f,** Schematic illustration of the difference in stability of Vn clusters in LC versus nLC states. **g,** Schematic diagram of enhancing cell response to mechanical cues by employing LC state to adsorb more Vn.
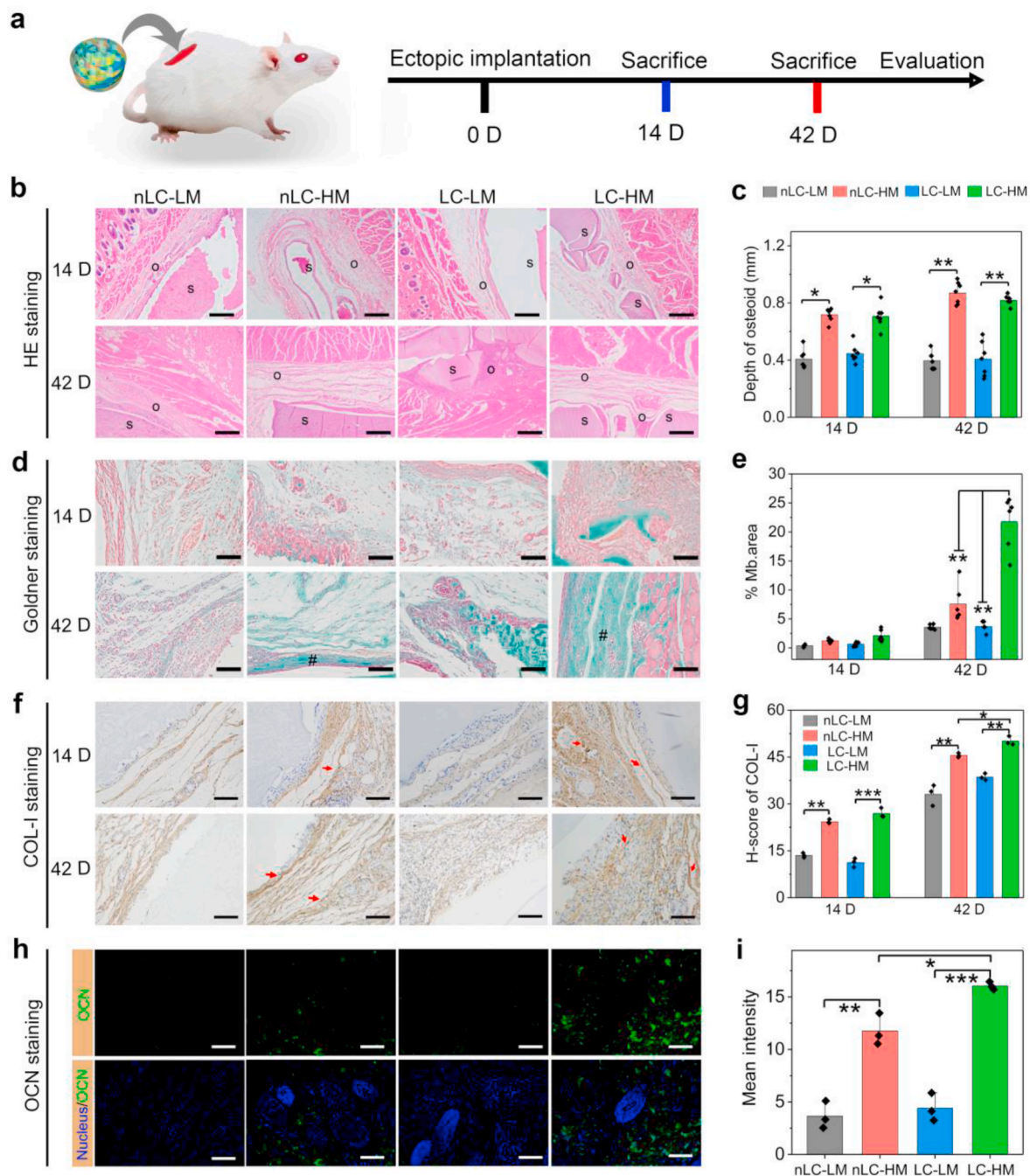
Fig. 8. **a,** *In vivo* evaluation of osteogenesis of the scaffolds after impanation in SD rat. Tissue section samples were obtained at 14 and 42 d **b,** Images of the HE staining at 14 and 42 d (S: scaffold, O: osteoid). Scale bar is 500 μm. **c,** Quantitative analysis of osteoid area in the HE immunohistochemical images (*$P < 0.05$, **$P < 0.01$, ANOVA, *n*=7). **d,** Images of the Goldner's trichromatic staining at 14 and 42 d (#: mineralized bone). Scale bar is 100 μm. **e,** Quantitative analysis of mineralized bone area in Goldner's trichrome immunohistochemical images (%Mb. area represents the ratio of mineralized bone area and view area) (*$P < 0.05$, **$P < 0.01$, ANOVA, *n*=6). **f,** Images of the COL-I immunohistochemical staining (a) at 14 and 42 d (red arrows: positive area). Scale bar is 100 μm **g,** Histochemistry score (H-score) of the COL-I. (*$P < 0.05$, **$P < 0.01$, ***$P < 0.001$, ANOVA, *n*=3). **h,** Immunofluorescence images of OCN (green) and nucleus (blue). Scale bar is **100 μm. i,** Mean fluorescence intensity of OCN of different groups at 42 d (*$P < 0.05$, **$P < 0.01$, ***$P < 0.001$, ANOVA, n = 3).

the scaffolds *in vivo* (Fig. S18). **Hematoxylin and eosin** (HE) images at 14 and 42 d post-implantation showed that the scaffolds were in good contact with the surrounding tissue (Fig. 8b), with no obvious inflammation. Some spindle-shaped cells around the scaffold were considered possible osteoid, and their thickness was measured to reflect the scaffold's effect on the tissues (Fig. 8c). The results indicated that the osteoid thickness of all high-modulus scaffold groups was greater than that of the low-modulus groups. However, since HE staining cannot specifically mark the osteogenic area, Goldner's trichrome staining was used to

further distinguish the mineralized area around the scaffolds (Fig. 8d). While there were few mineralized areas around the scaffold at 14 d, by 42 d, the mineralized areas became more prominent, and their areas were quantified (Fig. 8e). As expected, larger mineralized areas (green) appeared around the high-modulus scaffolds due to the improved mechanical microenvironment compared to the low-modulus scaffolds. More importantly, the mineralized area around the LC-HM scaffold was much larger than that around the nLC-HM scaffold, confirming the significant positive effect of LC state on osteogenesis. These results were

consistent with the *in vitro* evaluations. COL-I, an important component of the ECM secreted by osteoblasts, was monitored around the scaffolds (Fig. 8f). Obvious collagen fibers were observed around the scaffolds, and quantitative analysis (Fig. 8g) showed that the high-modulus groups had more COL-I compared to the low-modulus groups. The LC-HM scaffold had the highest H-score for COL-I, indicating strong osteogenic activity. OCN expression was observed through immunofluorescence staining. The OCN fluorescence intensities of the high-modulus groups were higher than those of the low-modulus groups (Fig. 8h). Quantitative analysis revealed that the LC-HM scaffold exhibited the highest OCN fluorescence intensity (Fig. 8i). This result implies that only in a high-modulus environment can LC state effectively promote bone formation. The high-modulus environment can activate the osteogenic properties of LC state, or perhaps LC state amplifies the osteogenic ability of the high-modulus environment. In summary, LC state and high-modulus microenvironment interact and synergistically promote OCN expression.

The *in vivo* osteogenic performance of different scaffolds was further evaluated through skull defect model. As shown in Fig. 9a, the rats were

sacrificed at 4 and 8 W respectively and the tissues and scaffolds were taken for morphological observation and staining. The micro-CT in Fig. 9b shows that there is almost no obvious bone formation in the central area of the defect at 4 W for all groups. Compared with the defect site at 4 W, there was a large number of new bone in the defect site at 8 W, and osteogenesis can be observed in the center of the bone defect, indicating that the reconstruction of the bone defect was accelerated. This result was also proven through quantitative analysis of micro-CT in Fig. 9c. The bone mineral density, trabecular number, and bone volume at 8 W were all higher than those at 4 W. Furthermore, through 3D reconstruction of the bone defect site, we found that there was obvious difference in the amount of new bone formation between the groups. Compared with the low-modulus groups, the high-modulus groups had more new bone ingrowth from the edges of the defect, which is consistent with the results of *in vitro* evaluation. In a high-modulus microenvironment, the LC scaffold obviously promoted the formation of more new bone, which means that the synergistic effect of LC state on osteogenesis was confirmed *in vivo*. HE staining was used to evaluate changes in surrounding tissue after scaffold implantation in Fig. 9d.
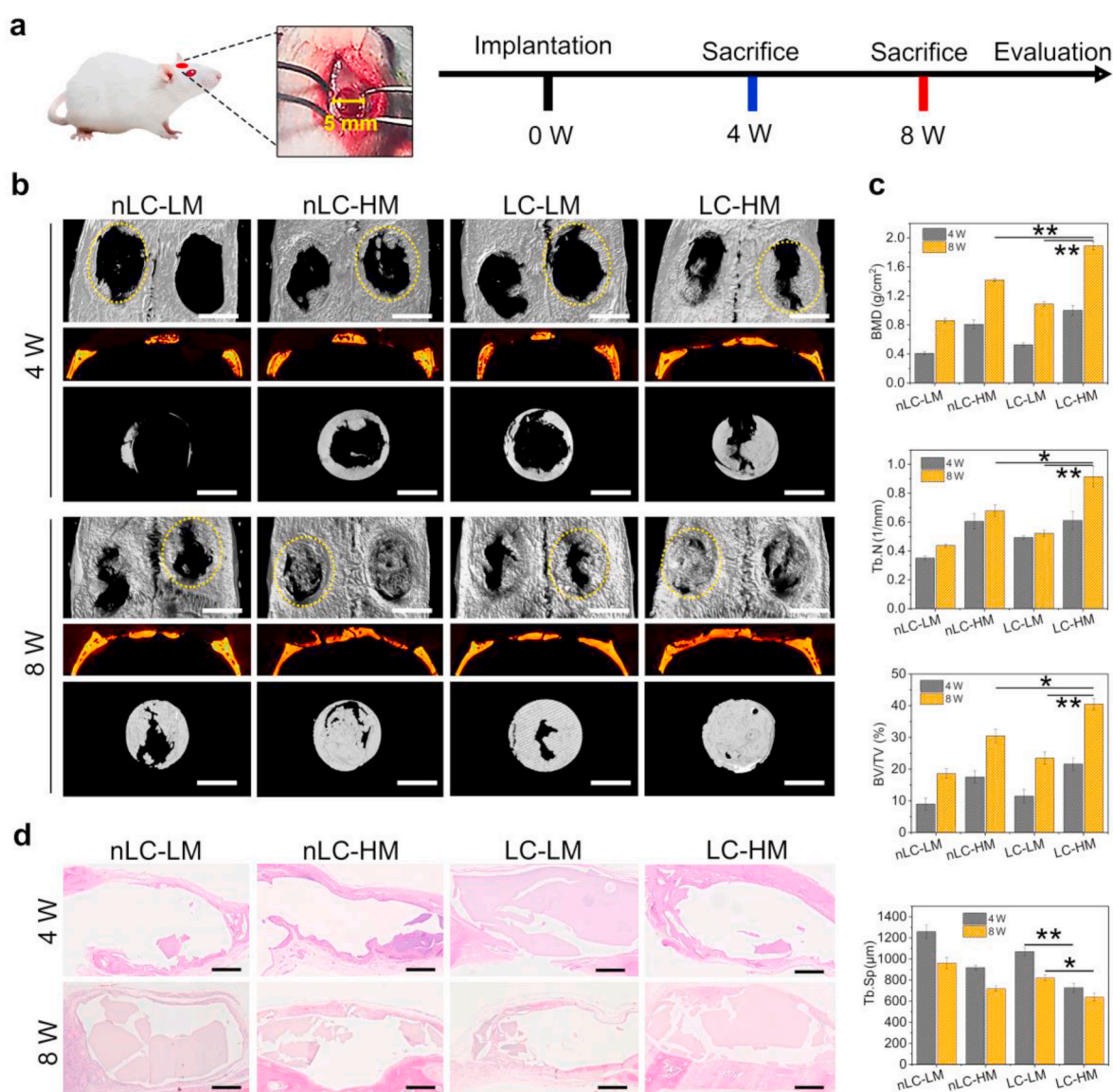
Fig. 9. a, Skull defect model of SD rats and pictures of the defects. Rats were sacrificed for evaluation at 4 and 8 W after implantation. b, Micro-CT analysis of bone formation at the defect sites (scale bar is 4 mm), central section and corresponding regions of interest (scale bar is 2 mm). c, The quantification of bone mineral density (BMD), bone volume/total volume (BV/TV), number of trabeculae (Tb.n) and trabecular separation (Tb.Sp) (*$P < 0.05$, **$P < 0.01$, ANOVA, $n = 5$). d, Images of the HE staining at 4 and 8 W. Scale bar is 400 μm.

After the scaffolds were implanted, there was no obvious inflammatory reaction in the surrounding area. Besides, we also noticed that the scaffolds were still presented in the defect site at 8 W and had not completely degraded.

The expression of OCN in new bone was further monitored by immunofluorescence, as shown in Fig. 10a. Regardless of whether it was 4 or 8 W, the images showed that the expression of OCN in the low-modulus groups was lower than that in the high-modulus groups. The same conclusion can be obtained from quantitative analysis in Fig. 10b. The effect of LC state on osteogenesis is also reflected through the expression of OCN. Compared with nLC-HM, the LC-HM group exhibits more positive areas, which means that LC state and viscoelasticity exert a synergistic effect in promoting osteogenesis. Goldner's trichrome staining was used to evaluate the mineralization of new bone. As shown in Fig. 10c & d, LC state and viscoelasticity show excellent properties in promoting mineralization. The mineralized area of the LC-HM group is the highest among all groups. In conclusion, *in vivo* skull defect evaluation demonstrated that the LC-HM scaffold had optimal osteogenic properties, which revealed that the viscoelasticity and LC state of the LC

hydrogel scaffold played a synergistic role in promoting mineralization and bone formation.

4. Conclusion

In summary, we presented 3D-printed hydrogel scaffolds with osteoid-like viscoelasticity and an LC state using pioneering LC inks, and we clarified the influence of osteoid characteristics in a 3D environment on cell behavior and osteogenesis both *in vitro* and *in vivo*. We found that compared to low-modulus scaffolds, high-modulus scaffolds significantly promote cell adhesion, spreading, and migration, leading to more actin filaments, higher traction, and greater cell polarity. Furthermore, high-modulus scaffolds facilitate the formation of focal adhesions and increase intracellular tension dominated by myosin-II, which activates the nuclear transfer of YAP. This, in turn, promotes the osteogenic differentiation and osteogenesis of BMSCs via YAP-dependent mechanotransduction, which can be regulated by adjusting the scaffold modulus. Interestingly, we also found that, compared to the non-LC state, LC state significantly enhances high protein clustering due to its unique chiral
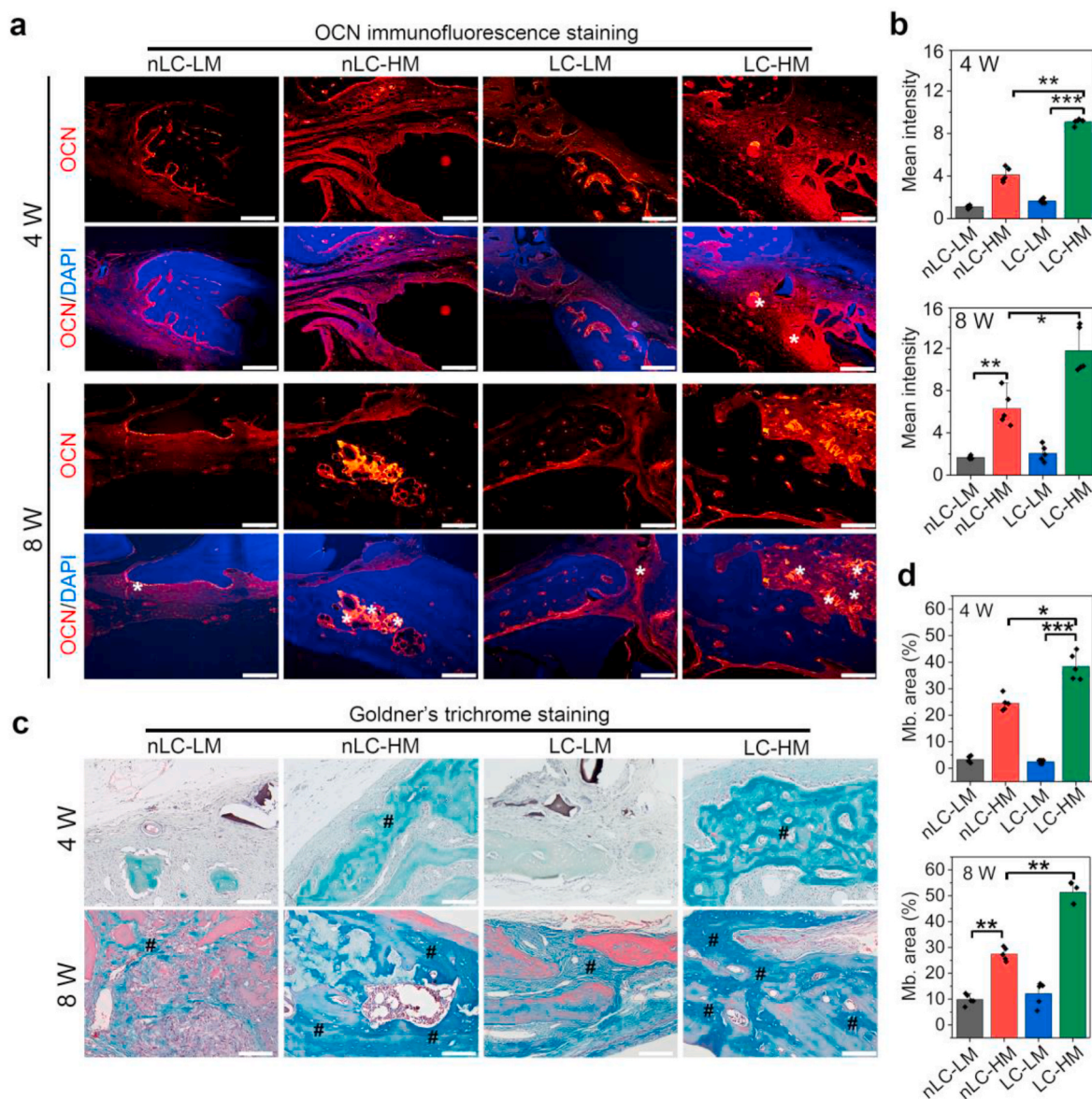
Fig. 10. a, Immunofluorescence images of OCN (red) and nucleus (blue) (*: positive area). Scale bar is 80 μm b, Mean fluorescence intensity of OCN of different groups at 4 and 8 W (*$P < 0.05$, **$P < 0.01$, ***$P < 0.001$, ANOVA, $n = 3$). c, Images of the Goldner's trichromatic staining at 4 and 8 W (#: mineralized bone). Scale bar is 100 μm d, The ratio of mineralized bone area and view area (*$P < 0.05$, **$P < 0.01$, ***$P < 0.001$, ANOVA, $n = 5$).

helical topological structure. More importantly, LC state-mediated high protein clustering can enhance focal adhesion formation and expose highly accessible RGD motifs, activating integrin receptors on the cell membrane. This enhances cell-protein interactions and promotes osteogenic differentiation. Notably, this positive role of LC state-mediated high protein clustering is more effective in high-modulus scaffolds than in low-modulus scaffolds, suggesting that LC state of the scaffolds does not act independently on the cells but synergistically with the viscoelastic microenvironment. *In vivo* evaluations further revealed the synergistic effects of LC state and viscoelasticity on osteogenesis. The results showed that LC state and viscoelasticity together promote bone formation, especially the expression of OCN and new bone mineralization. Taken together, our findings demonstrate that the viscoelasticity and LC state of osteoid amplify each other and mutually enhance cell adhesion and migration, regulating the osteogenic differentiation and osteogenesis of stem cells. This intriguing synergistic osteogenic effect of LC state and viscoelasticity contributes to our understanding of how 3D osteoid affects cell behavior and fate, providing fresh guidance for the construction of biomimetic scaffolds for future bone tissue engineering.

Conflicts of interest

There are no conflicts to declare.

Ethics approval and consent to participate

Ectopic osteogenesis: Male SD rats (Use permit: SYXK2020-0237, Ruige Biotechnology Co. Ltd) with an average weight of 200 g were used in this study All procedures were performed according to the approved guidelines of the local ethical committee for Animal Research (Approval No. IACUC HTSW220709).

Skull repair evaluation: Healthy male SPF rats with an average weight of 200 g were used in this study (Use permit: SYXK 2023-0307, Bes Test Bio-Tech Co,.Ltd.). All procedures were performed according to the approved guidelines of the local ethical committee for Animal Research (Approval No. IACUC B202310-13).

Data availability statement

The data that support the findings of this study are available from the corresponding author upon reasonable request.

CRediT authorship contribution statement

Kun Liu: Writing – review & editing, Writing – original draft, Visualization, Validation, Supervision, Software, Resources, Methodology, Investigation, Funding acquisition, Formal analysis, Data curation, Conceptualization. **Lin Li:** Validation, Formal analysis, Data curation. **Yizhi Li:** Data curation, Conceptualization. **Yiting Luo:** Investigation, Formal analysis, Data curation. **Zhaoyu Zhang:** Methodology, Investigation. **Wei Wen:** Software, Resources, Investigation. **Shan Ding:** Methodology, Investigation. **Yadong Huang:** Methodology, Investigation. **Mingxian Liu:** Methodology, Investigation, Formal analysis. **Changren Zhou:** Software, Resources, Methodology, Formal analysis. **Binghong Luo:** Writing – review & editing, Writing – original draft, Visualization, Validation, Supervision, Software, Resources, Project administration, Methodology, Investigation, Funding acquisition, Formal analysis, Data curation, Conceptualization.

Declaration of competing interest

The authors declare that they have no known competing financial interests or personal relationships that could have appeared to influence the work reported in this paper.

Appendix A. Supplementary data

Supplementary data to this article can be found online at https://doi.org/10.1016/j.bioactmat.2024.06.019.

References

[1] M.P. Lutolf, J.A. Hubbell, Synthetic biomaterials as instructive extracellular microenvironments for morphogenesis in tissue engineering, Nat. Biotechnol. 23 (1) (2005) 47–55.

[2] O. Chaudhuri, J. Cooper-White, P.A. Janmey, D.J. Mooney, V.B. Shenoy, Effects of extracellular matrix viscoelasticity on cellular behaviour, Nature 584 (7822) (2020) 535–546.

[3] J.M. Grolman, P. Weinand, D.J. Mooney, Extracellular matrix plasticity as a driver of cell spreading, Proc. Natl. Acad. Sci. USA 117 (42) (2020) 25999–26007.

[4] N. Huebsch, P.R. Arany, A.S. Mao, D. Shvartsman, O.A. Ali, S.A. Bencherif, J. Rivera-Feliciano, D.J. Mooney, Harnessing traction-mediated manipulation of the cell/matrix interface to control stem-cell fate, Nat. Mater. 9 (6) (2010) 518–526.

[5] A.J. Engler, S. Sen, H.L. Sweeney, D.E. Discher, Matrix elasticity directs stem cell lineage specification, Cell 126 (4) (2006) 677–689.

[6] C. Liu, Q. Yu, Z. Yuan, Q. Guo, X. Liao, F. Han, T. Feng, G. Liu, R. Zhao, Z. Zhu, H. Mao, C. Zhu, B. Li, Engineering the viscoelasticity of gelatin methacryloyl (GelMA) hydrogels via small "dynamic bridges" to regulate BMSC behaviors for osteochondral regeneration, Bioact. Mater. 25 (2023) 445–459.

[7] G. Chen, C. Dong, L. Yang, Y. Lv, 3D scaffolds with different stiffness but the same microstructure for bone tissue engineering, ACS Appl. Mater. Interfaces 7 (29) (2015) 15790–15802.

[8] K. Adebowale, Z. Gong, J.C. Hou, K.M. Wisdom, D. Garbett, H.-p. Lee, S. Nam, T. Meyer, D.J. Odde, V.B. Shenoy, O. Chaudhuri, Enhanced substrate stress relaxation promotes filopodia-mediated cell migration, Nat. Mater. 20 (9) (2021) 1290–1299.

[9] O. Chaudhuri, L. Gu, D. Klumpers, M. Darnell, S.A. Bencherif, J.C. Weaver, N. Huebsch, H.-p. Lee, E. Lippens, G.N. Duda, D.J. Mooney, Hydrogels with tunable stress relaxation regulate stem cell fate and activity, Nat. Mater. 15 (3) (2016) 326–334.

[10] F. Nudelman, K. Pieterse, A. George, P.H.H. Bomans, H. Friedrich, L.J. Brylka, P.A.J. Hilbers, G. de With, N.A.J.M. Sommerdijk, The role of collagen in bone apatite formation in the presence of hydroxyapatite nucleation inhibitors, Nat. Mater. 9 (12) (2010) 1004–1009.

[11] D. Eglin, G. Mosser, M.M. Giraudguille, J. Livage, T. Coradin, Type I collagen, a versatile liquid crystal biological template for silica structuration from nano-to microscopic scales, Soft, Matter 1 (2) (2005) 129–131.

[12] S. Nam, K.H. Hu, M.J. Butte, O. Chaudhuri, Strain-enhanced stress relaxation impacts nonlinear elasticity in collagen gels, Proc. Natl. Acad. Sci. USA 113 (20) (2016) 5492.

[13] K.M. Herbert, H.E. Fowler, J.M. McCracken, K.R. Schlafmann, J.A. Koch, T.J. White, Synthesis and alignment of liquid crystalline elastomers, Nat. Rev. Mater. 7 (1) (2022) 23–38.

[14] Z. Pei, Y. Yang, Q. Chen, E.M. Terentjev, Y. Wei, Y. Ji, Mouldable liquid-crystalline elastomer actuators with exchangeable covalent bonds, Nat. Mater. 13 (1) (2014) 36–41.

[15] J. Ma, Y. Yang, C. Valenzuela, X. Zhang, L. Wang, W. Feng, Mechanochromic, shape-programmable and self-healable cholesteric liquid crystal elastomers enabled by dynamic covalent boronic ester bonds, Angew. Chem., Int. Ed. 61 (9) (2022) e202116219.

[16] K. Liu, L. Li, J. Chen, Y. Li, W. Wen, L. Lu, L. Li, H. Li, M. Liu, C. Zhou, B. Luo, Bone ECM-like 3D printing scaffold with liquid crystalline and viscoelastic microenvironment for bone regeneration, ACS Nano 16 (12) (2022) 21020–21035.

[17] S. Tang, K. Liu, J. Chen, Y. Li, M. Liu, L. Lu, C. Zhou, B. Luo, Dual-cross-linked liquid crystal hydrogels with controllable viscoelasticity for regulating cell behaviors, ACS Appl. Mater. Interfaces 14 (19) (2022) 21966–21977.

[18] K. Liu, S. Tang, L. Zhu, W. Wen, M. Liu, H. Li, C. Zhou, B. Luo, Bio-inspired liquid crystal gel with adjustable viscoelasticity to modulate cell behaviors and fate, Composites Part B-Eng 234 (2022) 109704.

[19] K.H. Vining, D.J. Mooney, Mechanical forces direct stem cell behavior in development and regeneration, Nat. Rev. Mol. Cell Biol. 18 (12) (2017) 728–742.

[20] W. Liu, Q. Sun, Z.-L. Zheng, Y.-T. Gao, G.-Y. Zhu, Q. Wei, J.-Z. Xu, Z.-M. Li, C.-S. Zhao, Topographic cues guiding cell polarization via distinct cellular mechanosensing pathways, Small 18 (2) (2022) 2104328.

[21] B. Ercan, T. Webster, in: Nanotechnology and Regenerative Engineering, second ed., CRC press, Boca Raton, 2014.

[22] H.I. Chang, Y. Wang, Regenerative Medicine and Tissue Engineering - Cells and Biomaterials, Intech Open, Rijeka, 2011.

[23] Z. Tong, L. Jin, J.M. Oliveira, R.L. Reis, Q. Zhong, Z. Mao, C. Gao, Adaptable hydrogel with reversible linkages for regenerative medicine: dynamic mechanical microenvironment for cells, Bioact. Mater. 6 (5) (2021) 1375–1387.

[24] C.C. DuFort, M.J. Paszek, V.M. Weaver, Balancing forces: architectural control of mechanotransduction, Nat. Rev. Mol. Cell Biol. 12 (5) (2011) 308–319.

[25] J. Whitehead, K.H. Griffin, M. Gionet-Gonzales, C.E. Vorwald, S.E. Cinque, J. K. Leach, Hydrogel mechanics are a key driver of bone formation by mesenchymal stromal cell spheroids, Biomaterials 269 (2020) 120607.

[26] L. Li, K. Liu, J. Chen, W. Wen, H. Li, L. Li, S. Ding, M. Liu, C. Zhou, B. Luo, Bone ECM-inspired biomineralization chitin whisker liquid crystal hydrogels for bone regeneration, Int. J. Biol. Macromol. 231 (2023) 123335.

[27] Y. Wang, T. Azaïs, M. Robin, A. Vallée, C. Catania, P. Legriel, G. Pehau-Arnaudet, F. Babonneau, M.-M. Giraud-Guille, N. Nassif, The predominant role of collagen in the nucleation, growth, structure and orientation of bone apatite, Nat. Mater. 11 (8) (2012) 724–733.

[28] N.I. Nissen, M. Karsdal, N. Willumsen, Collagens and Cancer associated fibroblasts in the reactive stroma and its relation to Cancer biology, J. Exp. Clin. Cancer Res. 38 (1) (2019) 115.

[29] E. Charlier, C. Deroyer, F. Ciregia, O. Malaise, S. Neuville, Z. Plener, M. Malaise, D. de Seny, Chondrocyte dedifferentiation and osteoarthritis (OA), Biochem. Pharmacol. 165 (2019) 49–65.

[30] A.R. Armiento, M. Alini, M.J. Stoddart, Articular fibrocartilage - why does hyaline cartilage fail to repair? Adv. Drug Deliv. Rev. 146 (2019) 289–305.

[31] M.L. Zoch, T.L. Clemens, R.C. Riddle, New insights into the biology of osteocalcin, Bone 82 (2016) 42–49.

[32] M.A. Icer, M. Gezmen-Karadag, The multiple functions and mechanisms of osteopontin, Clin. Biochem. 59 (2018) 17–24.

[33] N. Rana, G. Privitera, H.C. Kondolf, K. Bulek, S. Lechuga, C. De Salvo, D. Corridoni, A. Antanaviciute, R.L. Maywald, A.M. Hurtado, J. Zhao, E.H. Huang, X. Li, E. R. Chan, A. Simmons, G. Bamias, D.W. Abbott, J.D. Heaney, A.I. Ivanov, T. T. Pizarro, GSDMB is increased in IBD and regulates epithelial restitution/repair independent of pyroptosis, Cell 185 (2) (2022) 283–298.e17.

[34] A. Elosegui-Artola, R. Oria, Y. Chen, A. Kosmalska, C. Pérez-González, N. Castro, C. Zhu, X. Trepat, P. Roca-Cusachs, Mechanical regulation of a molecular clutch defines force transmission and transduction in response to matrix rigidity, Nat. Cell Biol. 18 (5) (2016) 540–548.

[35] J.D. Humphrey, E.R. Dufresne, M.A. Schwartz, Mechanotransduction and extracellular matrix homeostasis, Nat. Rev. Mol. Cell Biol. 15 (12) (2014) 802–812.

[36] F. Reggiani, G. Gobbi, A. Ciarrocchi, V. Sancisi, YAP and TAZ are not identical twins, Trends Biochem. Sci. 46 (2) (2021) 154–168.

[37] C.G. Hansen, T. Moroishi, K.-L. Guan, YAP and TAZ: a nexus for Hippo signaling and beyond, Trends Cell Biol. 25 (9) (2015) 499–513.

[38] G. Halder, S. Dupont, S. Piccolo, Transduction of mechanical and cytoskeletal cues by YAP and TAZ, Nat. Rev. Mol. Cell Biol. 13 (9) (2012) 591–600.

[39] L. Wang, J.-Y. Luo, B. Li, X.Y. Tian, L.-J. Chen, Y. Huang, J. Liu, D. Deng, C.W. Lau, S. Wan, D. Ai, K.-L.K. Mak, K.K. Tong, K.M. Kwan, N. Wang, J.-J. Chiu, Y. Zhu, Y. Huang, Integrin-YAP/TAZ-JNK cascade mediates atheroprotective effect of unidirectional shear flow, Nature 540 (7634) (2016) 579–582.

[40] C.A. DeForest, D.A. Tirrell, A photoreversible protein-patterning approach for guiding stem cell fate in three-dimensional gels, Nat. Mater. 14 (5) (2015) 523–531.

[41] A.J. Zollinger, M.L. Smith, Fibronectin, the extracellular glue, Matrix Biol. 60–61 (2017) 27–37.

[42] B. Cheng, W. Wan, G. Huang, Y. Li, G.M. Genin, M.R.K. Mofrad, T.J. Lu, F. Xu, M. Lin, Nanoscale integrin cluster dynamics controls cellular mechanosensing via FAKY397 phosphorylation, Sci. Adv. 6 (10) (2020) eaax1909.